Numerical Investigation of Droplet Actuation via Electrowetting in Microchannels

Alborz Arzpeyma

A Thesis

in

The Department

of

Mechanical and Industrial Engineering

Presented in Partial Fulfillment of the Requirements
for the Degree of Master of Applied Science (Mechanical Engineering) at
Concordia University
Montreal, Quebec, Canada

August 2007

Library and
Archives Canada

Published Heritage
Branch

395 Wellington Street
Ottawa ON K1A 0N4
Canada

Bibliothèque et
Archives Canada

Direction du
Patrimoine de l'édition

395, rue Wellington
Ottawa ON K1A 0N4
Canada

Your file Votre référence
ISBN: 978-0-494-34681-5
Our file Notre référence
ISBN: 978-0-494-34681-5

NOTICE:
The author has granted a non-exclusive license allowing Library and Archives Canada to reproduce, publish, archive, preserve, conserve, communicate to the public by telecommunication or on the Internet, loan, distribute and sell theses worldwide, for commercial or non-commercial purposes, in microform, paper, electronic and/or any other formats.

The author retains copyright ownership and moral rights in this thesis. Neither the thesis nor substantial extracts from it may be printed or otherwise reproduced without the author's permission.

AVIS:
L'auteur a accordé une licence non exclusive permettant à la Bibliothèque et Archives Canada de reproduire, publier, archiver, sauvegarder, conserver, transmettre au public par télécommunication ou par l'Internet, prêter, distribuer et vendre des thèses partout dans le monde, à des fins commerciales ou autres, sur support microforme, papier, électronique et/ou autres formats.

L'auteur conserve la propriété du droit d'auteur et des droits moraux qui protège cette thèse. Ni la thèse ni des extraits substantiels de celle-ci ne doivent être imprimés ou autrement reproduits sans son autorisation.

In compliance with the Canadian Privacy Act some supporting forms may have been removed from this thesis.

While these forms may be included in the document page count, their removal does not represent any loss of content from the thesis.

Conformément à la loi canadienne sur la protection de la vie privée, quelques formulaires secondaires ont été enlevés de cette thèse.

Bien que ces formulaires aient inclus dans la pagination, il n'y aura aucun contenu manquant.

Canada

ABSTRACT

Numerical Investigation of Droplet Actuation via Electrowetting in Microchannels

Alborz Arzpeyma

In Lab-on-a-chip devices (LOC), the handling of fluid droplets is one of the most important issues. Among all the ways of microactuation, electrowetting has been shown as a reliable actuation method in digital microfluidics. Its major advantages are the absence of heat generation, a rapid switching response, flexibility, and low power consumption. While most studies have been directed at performing experiments, numerical simulations of the phenomenon and its application to the design of LOCs are very few and there is still much work to do.

In the current work, a numerical study has been performed to simulate droplet behaviour under electrowetting actuation. Due to the presence of the droplet in the domain, a free surface flow problem must be solved. A Volume of Fluid (VOF) technique is applied to track the interface. In addition, due to the variable nature of the applied electric field, the relevant equation should be solved in time and space. The flow is considered laminar and Newtonian and all equations are solved in three dimensions.

Several aspects of droplet morphology are studied: contact line deformation, onset of actuation, and droplet deformation at different stages of actuation process. The droplet velocity is studied in detail and the numerical results are validated by existing experimental data in the literature. A velocity of 22 mm/s is achieved for the actuation voltage of 60 V. For design purposes, other parameters such as the electrode switching frequency and the electrode length effect on droplet velocity were also studied.

Acknowledgements

I would like to thank my supervisors Dr. Ali Dolatabadi and Dr. Paula Wood-Adams at Concordia University who helped me though this research. I also thank my colleague Shan Bhaseen who helped me with some of the simulations.

I would like to acknowledge Simulent Inc., Toronto, Ontario for providing access to the SIMULENT code which is modified for the present simulations and also the financial support by Natural Sciences and Engineering Research Council (NSERC) and Le Fonds québécois de la recherche sur la nature et les technologies (FQRNT).

Table of Contents

List of Figures

Notations

A_{SL}	solid-liquid interface area
C	capacitor
d	insulator thickness
D	electric flux density
E	electric field
F	electrode switching frequency
F_b	body forces
F_{ST}	surface tension volumetric force
f	volume fraction
g	gravitational acceleration
$\hat{n}$	unit normal vector
p	pressure
R	radius of curvature
S	interface area
t	time
Δt	timestep
u	velocity in x direction
v	velocity in y direction
V	velocity
V'	interim velocity
w	velocity in z direction
Δx	grid size in x direction
Δy	grid size in y direction
Δz	grid size in z direction

Greek letters

α	polar angle
χ	susceptibility
ε_0	permittivity of the air
ε_I	dielectric coefficient of the insulator
γ_{LG}	surface energy at liquid-gas interface
γ_{SG}	surface energy at solid-gas interface
γ_{SL0}	initial surface energy at solid-liquid interface
γ_{SL}	surface energy at solid-liquid interface
μ	viscosity

θ	contact angle after actuation
ρ	fluid density
σ	surface charge density
$\tilde{\tau}$	shear stress tensor
Ω	grid cell volume
ψ	electric potential
ψ_0	electric potential of the electrode
$\tilde{\psi}$	Electric potential at the interface

Subscripts and superscripts

i,j,k	grid number
l,m,n	grid number
n	timestep
new	new value
old	old value

1. Introduction

Through the past decades, rapid improvements in technology have facilitated the fabrication of miniaturized instruments leading to a boom in the development of Microelectromechanical devices (MEMS). Also, pressure sensors and other mechanically moveable structures and fluid handling devices were developed including channels (capillary connections), mixers, valves, pumps, and dosing devices.

At the beginning of the 1990s, Lab-on-a-chip (LOC) devices started to become a special interest. The first studies were devoted to the development of micropumps, flow sensors, and concepts for integrated fluid treatments for analysis systems. The goal was to replace the room-sized laboratory with a credit card-sized one. The advantages of the LOCs are remarkable reductions in the amount of required samples and reagents, shorter reaction and analysis time, high throughput, automation and portability.

A lab-on-a-chip device is a small biological or chemical laboratory, usually around few centimeters by few centimeters in area, built on a thin glass or plastic plate. It can consist of microchannels, microvalves, pumps, sensors, and electric circuits.

Liquids are the most important media in biomedical analysis and diagnostics. The liquids involved are often whole blood samples, protein or antibody solutions, and various buffers. A lab-on-a-chip device is expected to do the following microfluidic tasks: pumping, metering, mixing, flow switching, thermal cycling, sample dispensing or injection, and separating molecules and particles [1].

Some specialized applications of the LOC's were to develop an integrated DNA analysis device in which the droplet was driven through a thermal chamber and into electrophoresis chamber for analysis [2,3,4,5].

1.1 Continuous and digital microfluidics

Most technologies use continuous flow through microchannels, which are fabricated from glass or plastic. There are several ways to pump the liquid such as applying external pressure source, integrated mechanical micropumps, and electrokinetic mechanisms. In these systems, the sample reagents are loaded into one end and move toward the output which is at the other end. Between these two points different tasks may be performed such as mixing, sample injection, and separation. Although these systems are sufficient for many simple applications, they are not capable of performing more complex tasks which need high degrees of flexibility or complicated fluid manipulation.

The difficulty in dealing with the continuous flows comes from the fact that the governing parameters of the flow field, e.g. pressure, fluid resistance, and electric field, vary along the flow-path, and as a result, at each location in the system the flow is dependent on these properties. In the case of flow mixing and reaction, the problem becomes more complicated and the flow behaviour becomes more unpredictable due to the changes in electrical and hydrodynamic properties. As a result, the design and analysis of such systems is challenging. Such fabricated systems are suitable only for a narrow class of applications, as the structure and function are tightly coupled.

A way to resolve this problem is the application of discrete and independently controllable droplets. This method allows for a repeated pattern of cells and connectors which can be used for the small sets. Combination of these small sets may be used to generate larger sets. Therefore, the design and analysis of arbitrary complex microfluidic systems becomes feasible. Such cells may be reorganized both through hardware and software, to attain new functionality. Thus, digital microfluidic systems are flexible, scalable, and reconfigurable. In addition, there is no need for excess fluid to fill the microchannel, so the amount of required sample and reagent decreases.

Surface tension gradients are capable of producing bulk flow of liquid films or droplets. Such flows, called Maragoni flows, may be due to chemically or thermally induced surface tension gradients within a liquid meniscus. More precisely, the Maragoni flow is a surface flow which results in a bulk flow, and surface tension actuation may be used as a direct driving force for the bulk flow of liquid droplet inside microchannels.

1.2 Actuation principles in microfluidics

In order to study actuation phenomenon, the droplet energy balance needs to be analyzed. For this reason, a droplet at rest on a hydrophobic surface is considered. Due to the very small scales, the gravity force is neglected. The force at the solid-liquid-gas interface or the tri-phase contact line may then be described by Young's equation:

$$\gamma_{SG} - \gamma_{SL} = \gamma_{LG} \cos\theta \tag{1-1}$$

In this relation γ_{SG}, γ_{SL}, and γ_{LG} are the solid-gas, solid-liquid, and liquid-gas surface energies respectively. This relation may be easily obtained by writing the surface energy balance. Figure 1-1 shows the surface forces and the droplet sitting on the solid substrate. At equilibrium, the force balance imposes a droplet contact angle θ on the solid substrate.

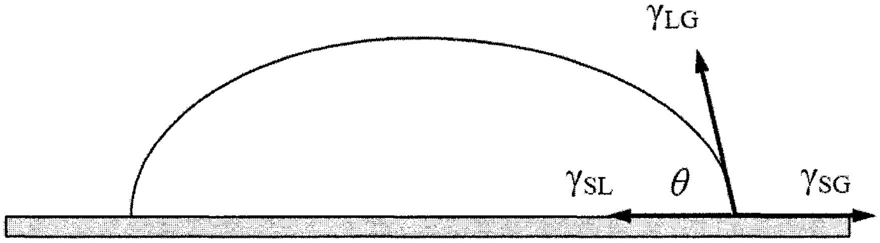

Figure 1-1. The equilibrium forces on one side of non-wetting droplet at rest on a solid substrate

In the case of capillary rise where a small capillary of radius r placed in a pool of liquid exposed to the atmosphere, $\cos\theta$ is positive. The liquid rises in the capillary decreasing the lower energy solid-gas interface and increasing the higher energy solid-liquid. The total energy reduction is $(\gamma_{SG} - \gamma_{SL})2\pi rh$, where h is the distance the liquid rises in the capillary. The work done to raise the column of liquid is $\Delta P \pi r^2 h$ which balances the energy reduction. Combining the two equations yields the Young-Laplace equation:

$$\Delta P = \frac{2(\gamma_{SG} - \gamma_{SL})}{r} = \frac{2\gamma_{LG}\cos\theta}{r} \tag{1-2}$$

For an arbitrarily curved surface, the general form of Equation (1-2) is:

$$\Delta P = \gamma\left(\frac{1}{R_1} + \frac{1}{R_2}\right) \tag{1-3}$$

where γ is the surface tension and R_1 and R_2 are the surface curvature radii. Equations (1-1), (1-2), and (1-3) are the basic equations for the surface tension and capillary phenomenon.

When a droplet is in contact with a surface, exhibiting a surface energy gradient, it imposes a contact angle gradient which causes an imbalance in the surface tension forces acting on the contact line. This case is shown in Figure 1-2. Such a force may induce bulk flow of the droplet. One of the earliest demonstrations of this principle was shown by Chaudhury and Whitesides [6] where they produced a smooth gradient of surface energy by exposing a silicon wafer to a diffusing front of decyltrichlorosilane vapor. The droplets of water placed at the more hydrophobic end of the wafer, inclined 15°, moved up toward the hydrophilic end with a velocity of 1-2 mm/s. In a similar case, where the droplet is limited in a capillary or channel (Figure 1-3), the gradient of liquid-gas interfacial energy may generate a force on the droplet. This force may be easily calculated from Equation (1-2).

A gradient in surface tension may cause motion of the droplet, if contact angle hysteresis is not significant. In reality, contact lines are characterized by a range of contact angles rather than a single equilibrium one [7,8] which is known as contact angle hysteresis. A recently advanced contact line has a higher contact angle θ_A than a recently receded one with the angle θ_R. Since at equilibrium, the contact angle has a value between these two upper and lower cases, an additional force is needed to start the droplet motion. Currently, studies are being performed on this field, however, the origins of contact angle hysteresis are not well-understood. Its majors causes are believed to be associated with roughness and heterogeneity of the surface [9 ,10].

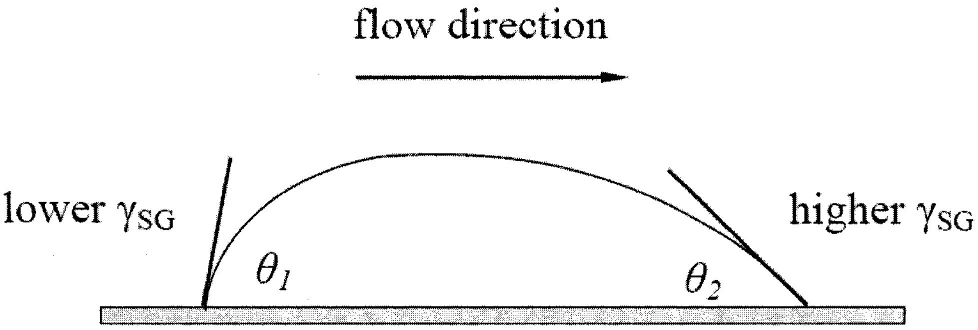

Figure 1-2. Surface energy gradient in a droplet at rest

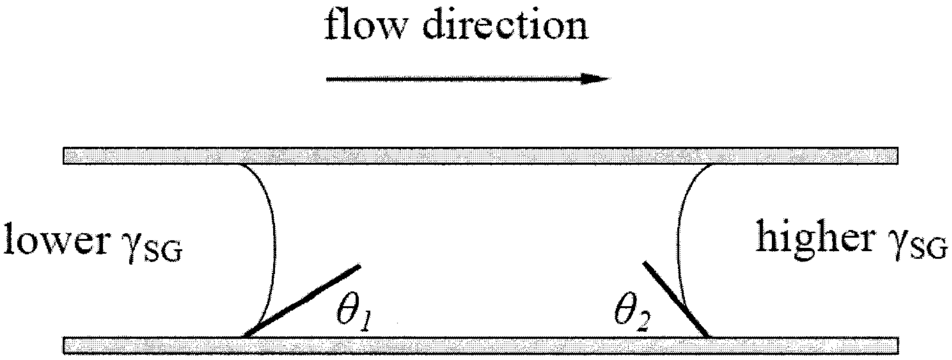

Figure 1-3. Droplet in a capillary, The menisci surface energies are different

1.3 Droplet actuation by surface tension forces

There are different ways to actuate liquid inside microchannels. Some examples are the application of air pressure, thermocapillary effects, electrochemical methods, electromechanical approaches. Most of these methods are based on the change in surface tension force as in the microdomain, these forces are dominant. A surface tension change may be generated by chemical, thermal or electrical methods, each will be briefly described below.

1.3.1 Chemical methods

In the electrochemical method, the surface tension gradient is generated along a channel by the application of redox-active surfactants. Gallardo et al [11] proposed this method. The surfactant is oxidized at one electrode and reduced it at another to generate a concentration gradient. This gradient is then capable of driving the liquid droplets in a simple fluidic network with a moderate velocity of about 2.5 mm/s using a low voltage of less than 1 *V*. However, the limit to this method is that the liquid should be insoluble in the electrolyte solution, in other words, it is suitable only for non-aqueous liquids. In addition, it is not convenient to control different droplets independently since the electromechanical gradient is generated along the whole channel length.

Another method is the application of light to generate a surface tension gradient. This is known as the photochemical method. Although it is convenient to control the two-dimensional movement of separate droplets on a chip without the fabrication of a microstructure, the reported velocities are very small; 50 μm/s [12]. This shows that the force generated is small and often not enough to overcome the contact angle hysteresis of many liquids such as water.

1.3.2 Thermal methods

Thermal methods are more promising than the chemical ones. The idea is to heat the ends of a droplet in a capillary thereby producing a surface tension gradient which actuates the droplet. The surface tension of a liquid meniscus decreases with increasing the temperature. This method has been well-studied [13,14] and applied in simple DNA analysis devices [3,4]. The advantage of this method is that the droplets can be independently controlled if there are multiple independently controlled microheaters in the microchannel. The disadvantage of this method is that the design is complicated since a complete heat transfer analysis is required which is dependent on several factors such as substrate type, channel geometry, and fluid type and velocity [14]. In addition, a relatively high temperature gradient is needed to actuate the droplet. As an example, a temperature difference of 20 – 40 °C is required to initiate movement of a water droplet. Such temperature changes are unacceptable for many potential biological applications where the temperature should remain almost constant.

1.3.3 Electrical methods

The change in the interfacial tension between two fluids was first studied by Lippman [7] about 125 years ago. He studied the electrocapillary effect in which the height of a mercury column in contact with an electrolyte can be controlled by means of an electric potential. This method has the same problem of not being able to control multiple droplets independently as it is necessary to apply the electric voltage to both the droplet and the surrounding medium. In addition, the phenomenon is strictly dependent on the electric double layer EDL at the interface, which means it is highly dependent on the type and concentration of the electrolyte in the aqueous phase.

The idea of continuous electrowetting (CEW) was introduced later on [15]. In this method, a droplet of a liquid metal is actuated by an external electric field along the whole channel length. The capillary is filled with an electrolyte. A surface tension gradient is generated by the electrostatic gradient due to the resistance of the electrolyte in the gap between the droplet and the capillary wall. The actuation force was remarkable and the velocities of up to 10 cm/s were achieved. The CEW system was applied in many instruments [16,17] but the same problem of the classical electrocapillary persisted.

Steps have also been taken to achieve independently actuated droplets. Washizu [18] studied a system of a series of electrodes in a hydrophobic insulator. The electrostatic attraction between the conductive droplet and the electrode induced motion. He developed a microreactor to transport and sort and fusion of different droplets of 0.5 - 5.0 μl. Relatively small velocities of about 400 μm/s were attained. This method has similarities with the electrowetting method that appeared later on, though it is not completely dependent on the electrical control of surface tension.

Another electrical method to actuate the droplets is electrowetting. In this method the interfacial solid-liquid energy is changed by the application of an external electric field. As oppose to the other electrical methods where the interface is between two liquids, in electrowetting, there is a solid phase engaged that makes it possible to precisely control the interfacial energy. The system can contain a series of electrodes which are each independently controlled (Figure 1-4). As a result, several droplets may be controlled in a precise way through a single system. This makes it quite flexible and useful for digital microfluidics.

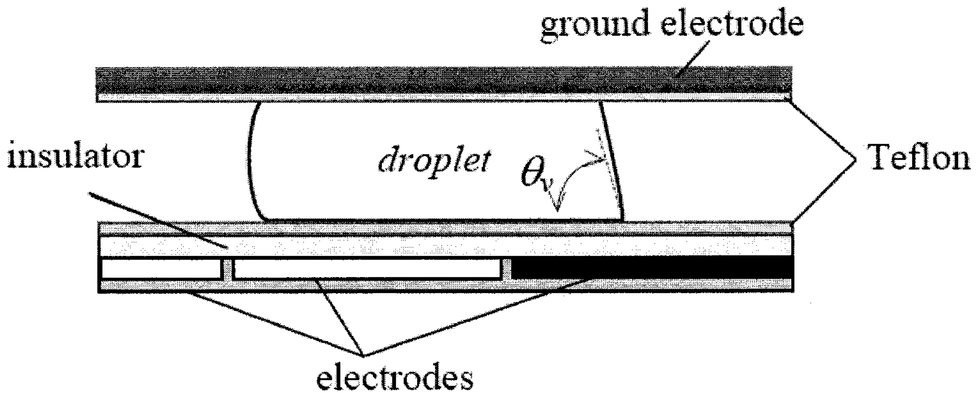

Figure 1-4. Electrowetting actuation of droplet along a channel, the powered electrode is shown darker

In this method, the electrical energy is stored in the solid-liquid interface at one end of the droplet. The droplet initially rests on a hydrophobic surface and then starts to stretch toward where the powered electrode is located. The extra energy decreases the interfacial energy leading to a decrease in the solid-liquid contact angle. As a result, the hydrophobic surface turns to a hydrophilic one at the electrode location. A detailed explanation of this method is presented in the second chapter.

Due to the advantages and flexibilities of this method in digital microfluidic, electrowetting has been studied widely recently. A remarkable number of these studies are experimental ones. Tests have been performed to investigate the capacity and flexibilities of the electrowetting-based instruments. Pollack et al [19,20] performed detailed experiments in this field. They achieved a droplet velocity of 10 cm/s with the actuation voltage of 60V. Different media may be used as the fluid in which the droplet is immersed. Experiments demonstrate that by applying the electric potential, the droplet starts to deform. However, a certain voltage needs to be attained in order for droplet movement to begin. This voltage is called the threshold voltage. Pollack et al [19,20] investigated two different surrounding media: air and silicon oil. The threshold voltage for the system with a droplet immersing in silicone oil is noticeably less than the one in air. In addition, the effects of electrode pitch and channel gap on the threshold voltage were investigated. They demonstrated that the method may be used for droplet transport as well as droplet dispensing and manipulation. By using a specific array of electrodes different tasks may be performed such as droplet mixing, merging, cutting, and splitting [21,22]. Also the system shows a very good accuracy which makes it possible to dispense a precise amount of a liquid from a reservoir. These characteristics are favorable for lab-on-a-chip devices and facilitate handling of droplets of biochemical agents and DNA. In summary, the advantages of this technique include the absence of heat generation, rapid switching response, flexibility, and low power consumption.

Along with the experimental studies, analytical and numerical studies have been done to explain the phenomenon. There are mainly three methods to derive the electrowetting equations which will be further explained in Chapter 2 and the Appendix. The forces were derived for the case in which the droplet is in the equilibrium condition sitting on a substrate [23,24] and also the case for which the droplet is moving along a channel. In the second case, a series of electrodes is involved. As a result, the droplet that moves in the domain, changes the electric field pattern inside the channel. Also, the electrodes need to be switched successively so that the actuation force is continuous. A capacitance model has been developed based on an energy minimization method for this case [25]. In these analytical studies, the electrostatic force and charge distribution both at the liquid-gas interface and tri-phase contact line have been studied for the advancing and receding fluid faces [26]. Also the maximum and minimum voltage that is needed to actuate the droplet has been calculated analytically [27].

Dolatabadi et al. [28,29,30] performed numerical simulations to predict the droplet behaviour under electrowetting actuation. They applied a direct method to change the contact angle based on its relation with the applied voltage and the contact angle is considered constant at the location defined for the electrodes. Their results show acceptable consistency with the experiments, however, a more precise model is needed to accurately predict the droplet behaviour. In particular, they assumed an array of infinitesimal electrodes which over predicts the droplet velocity.

Despite the large number of experimental studies in this field, very few numerical simulations have been performed. In reality, doing many experiments can be difficult, costly and time consuming. Usually the Teflon covering of the substrates is destroyed after several cycles of actuation and needs to be recoated. Also, the mounting of the electrode on the substrates is difficult. Currently, as the experimental device and its parts are very small in scale, system preparations and handling becomes more difficult. Thus, it is quite favorable to develop a numerical technique which is capable of simulating the system more precisely. In such a case, the number of experiments decreases noticeably. The numerical simulations may also help to study different aspects of droplet transport and manipulation to suggest further experiments. Unfortunately, in current literature, there is not much work that has been done to develop the simulation.

1.4 Objectives

The objective of this work is to develop an accurate numerical model to simulate the droplet behaviour under electrowetting actuation from first principles. To do this, the electrohydrodynamics aspects of the problem are considered and the electric forces acting on the fluids are derived. Their effect on the contact angle is studied with respect to time and space. This allows further studies on the droplet behaviour which is a crucial issue in the design process.

The next chapter is dedicated to the principles of electrowetting, the required mathematical formulation which explain the phenomenon. The flow governing equations along with the electric field equation, their discretization, the required initial and boundary conditions, and the numerical approach to solve them are discussed in chapter 3.In chapter 4, the results are presented. Different aspects are studied such as the droplet actuation procedure, droplet morphology, its velocity, and the effects of electrode switching frequency and electrode length on droplet motion along the channel.

2. Electrowetting

As it is discussed in the first chapter, electrowetting is a reliable means of actuation in digital microfluidics. The concept of electrowetting is to change the interface energy by applying an external electric field. This leads to a higher charge concentration in the tri-phase contact line which affects the surface tension force. As a result, the energy balance of the system changes. Figure 2-1a shows a schematic of a droplet in equilibrium on a hydrophobic surface. As it may be observed, the contact angle is large. By applying a voltage, the solid-liquid interface energy decreases (Figure 2-1b). In order for the droplet to adapt to the new energy balance, the liquid-solid interface contact angle decreases and the droplet stretches over the surface. In this condition, the surface is hydrophilic.

At equilibrium, we can write the following energy balance:

$$\gamma_{SG} = \gamma_{SL} + \gamma_{LG} \cos\theta \qquad (2\text{-}1)$$

This equation is known as Young's equation which explains the relation between the surface energies and the contact angle.

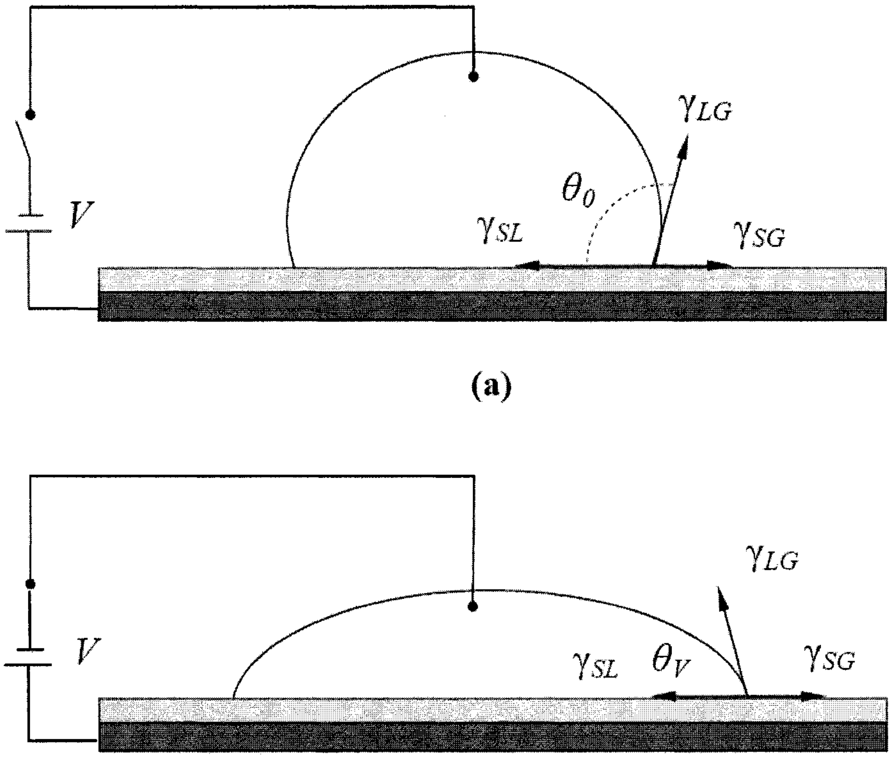

(a)

(b)

Figure 2-1. Schematic of the droplet: (a) not actuated; (b) in the presence of the electric potential

The liquid is neutral, having the same amount of ions and counter ions. However, under an electric field the charges at the solid substrate attract the ions in the liquid. Therefore, the charge concentration increases in the vicinity of the solid substrate to balance the substrate charges. Immediately adjacent to the charged solid surface, there is a layer of ions strongly attracted to the solid surface which is called the compact layer. From the compact layer to the electrically neutral bulk fluid, the charge density gradually reduces to zero. This layer is called the diffuse layer and together with the compact layer it makes the electric double layer, EDL. Figure 2-2 is a schematic of the EDL with the compact and diffuse layers. The thickness of the compact layer is normally on the order of several Angstroms [1]. The total thickness of the EDL is about 10-100 nm [31].

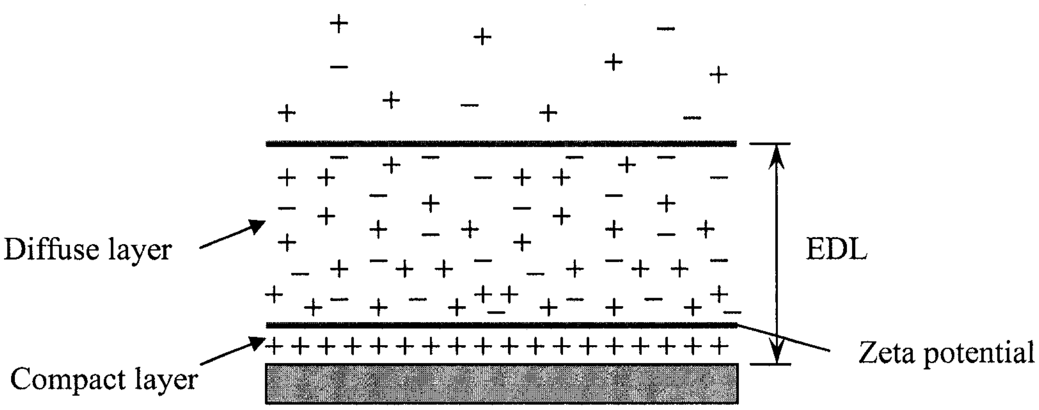

Figure 2-2. EDL, consisting compact and diffuse layers.

The thickness of the EDL is normally very small and does not store much energy. In order to increase the energy stored in the system, a dielectric covering is used on the electrodes. This is called Electrowetting on Dielectric, EWOD. Since the energy stored in the dielectric is much more than the one that is stored in the EDL, the effect of electric double layer may be neglected in modeling the phenomenon.

There are different approaches to study the electrowetting phenomenon: the capacitance model, the energy minimization method, and the electromechanical approach. The capacitance model is discussed in detail in the following section. The two other methods are discussed briefly in the Appendix.

2.1 Capacitance model

One of the approaches which has been suggested to model the electrowetting effect is to consider the system as a capacitor. Then, the electric energy is calculated by the energy stored in a capacitor and added to the Young's equation (Equation (1-1)). The presence of an external electric field affects the free charges in the liquid which leads to their rearrangement. The resultant Coulombic force in the interface is the driving force for the liquid.

The conductive droplet is placed on a hydrophobic surface. A positive electrode, mounted below the plate, and the top ground electrode together with the conductive droplet form the capacitor (Figure 2-3).

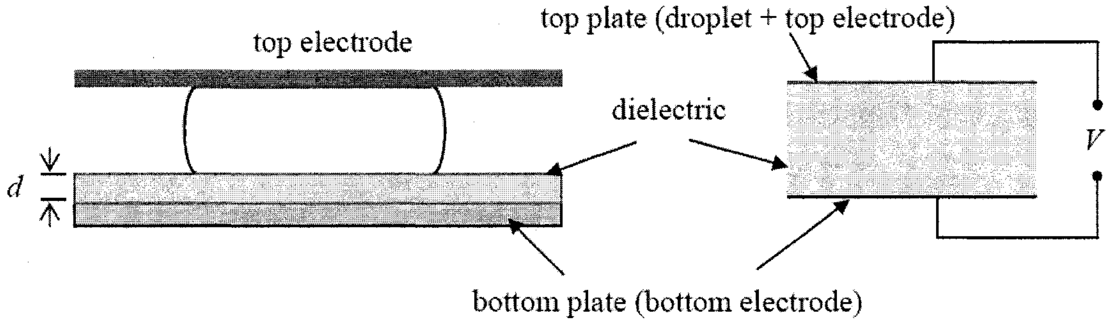

Figure 2-3. Capacitor model

Electrowetting originates from the presence of free charges at the solid-liquid interface. The droplet is in contact with an electrode but there is no current crossing the droplet-solid interface. The free charges on both sides of solid-liquid interface form a parallel plate capacitor in which the gap is the electric double layer (EDL). In electrowetting on dielectric, the gap is a thin layer of insulating material between the liquid and solid phases. In this research, a layer of Parylene C is considered as the dielectric and the capacitor approach is used to model the electrowetting phenomenon. The energy stored in the dielectric layer may be calculated as:

$$E = \frac{1}{2} C \psi^2 = \frac{\varepsilon_0 \varepsilon_l}{2d} \psi^2 \tag{2-2}$$

In this relation $\varepsilon_0 \varepsilon_l$ is the dielectric constant of the insulator layer, d is the dielectric thickness, and ψ is the applied voltage. By combining this stored energy with the energy balance equation (Young's equation (1-1)), a new relation is obtained:

$$\cos\theta(V) = \cos\theta_0 + \frac{\varepsilon_0 \varepsilon_l}{2d\gamma_{LG}} \psi^2 \tag{2-3}$$

Equation (2-3) called the Young-Lipmann equation, is the relation between the actuated contact angle $\theta(V)$ and the applied voltage ψ. θ_0 is the non-actuated contact angle which is the contact angle of the droplet sitting on a solid surface before applying the voltage. This angle for the case of a water droplet on Teflon is 104°.

This concept may be adopted to make a droplet move along a microchannel. In this case, an array of electrodes is needed on one of the plates (top or bottom) and the other plate remains grounded. Figure 2-4 shows an array of electrodes used to actuate the droplet. To make the droplet move inside the channel, the right electrode is switched on (darker electrode), while all other electrodes are off. This leads to a decrease in surface energy at the leading edge which consequently decreases the solid-liquid contact angle. As there is no direct actuation at the droplet trailing edge, the contact angle is expected to remain constant. This contact angle difference which comes from the imbalance in surface energies at the two edges generates a force towards the right which is called the electrowetting force. By switching the electrodes successively, it is possible to move the droplet inside the channel.

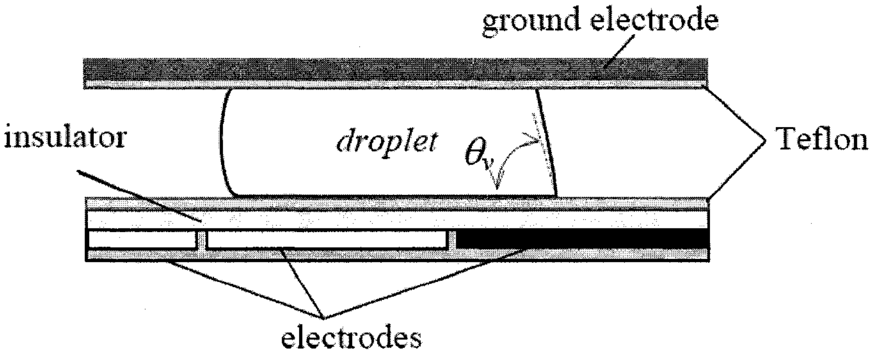

Figure 2-4. Schematic of droplet actuation in a microchannel

To calculate the electric force acting on the droplet, the electric field should be calculated inside the channel. The location of the electric source, which is the powered electrode, changes with time, and also the droplet position inside the channel, affects the electric field pattern in the domain. Therefore, the electric forces acting on the droplet vary with time and space. In order to capture these variable forces, the electric field should be calculated for each time and at each point in space.

2.2 Electric Field Formulation

The electric field inside the domain may be formulated from Maxwell's first equation. Based on Gauss's law, the total electric flux through a closed surface is equal to the charge enclosed in the domain:

$$\oint_s \vec{D}\cdot d\vec{s} = \int_{Vol} \rho_V dV \quad \text{or} \quad div\vec{D} = \rho_V \qquad (2\text{-}4)$$

In this equation $\vec{D}$ is the electric flux density and ρ_V is the volumetric electric charge density. The relation between the electric flux and the electric field depends on the material in which the electric field penetrates. For electrically linear materials, such as water without biochemical agents, the relation can be written as:

$$\vec{D} = \varepsilon_0 (1 + \chi)\vec{E} \tag{2-5}$$

ε_0 is the permittivity of free space and χ is susceptibility. Equation (2-5) may be written in a simpler way as:

$$\vec{D} = \varepsilon_0 \varepsilon \vec{E} \tag{2-6}$$

where $\varepsilon_0 \varepsilon$ is the dielectric constant of the material which is the Parylene C covering layer in this case. In addition, the relation between the electric potential and the electric field is known:

$$\vec{E} = -\nabla \psi \tag{2-7}$$

By combining the above equations, the differential equation is obtained to calculate the electric potential inside the domain. In fact, the equation is a Poisson equation and may be written as:

$$\nabla^2 \psi = -\frac{\rho_V}{\varepsilon_0 \varepsilon} \tag{2-8}$$

Here the right hand side of the equation is the bulk charge density. In the cases where there is no free charge, the Poisson equations simplifies to the well-known Laplace equation:

$$\nabla^2 \psi = 0 \tag{2-9}$$

This assumption is valid for our case. As electrowetting deals with rearranging the surface charges, there is no extra charge added or removed from the system. Thus, to calculate the electric potential in the domain we need to solve the Laplace equation with proper boundary conditions.

The two other approaches which will be explained briefly in Appendix are identical in the final results. In this research, the capacitor approach is considered to model the phenomenon and the solid-liquid contact angle is calculated at each point which is then applied as contact angle constraints to the flow equations.

3. Numerical Approach

In this chapter the flow equations that are to be solved are explained. In addition, the discretization, the boundary conditions, and the numerical scheme applied to solve these equations are discussed. The governing equations for this specific problem consist of two parts:

- Flow governing equations
- Electric potential equation

The flow governing equations are discussed in section below while the electric potential equation solution is discussed in Section 3.3.

3.1 Mathematical formulation

The following assumptions are considered in all simulations:

- The liquid phase is considered incompressible and Newtonian.

- The flow is considered laminar.
- The equations are discussed and solved in three dimensions.

3.1.1 Governing equations

The mass and momentum conservation equations in the liquid phase may be written as:

$$\nabla \cdot \vec{V} = 0 \tag{3-1}$$

$$\frac{\partial \vec{V}}{\partial t} + \nabla \cdot \left(\vec{V}\vec{V}\right) = -\frac{1}{\rho}\nabla p + \frac{1}{\rho}\nabla \cdot \tau + \vec{g} + \frac{1}{\rho}\vec{F}_b \tag{3-2}$$

$\vec{V}$ is the velocity vector, p the pressure, ρ the liquid density, $\tilde{\tau}$ the shear stress tensor, $\vec{g}$ gravitational acceleration, and $\vec{F}_b$ any body forces (per unit volume) acting on the fluid. As the fluid is Newtonian:

$$\tilde{\tau} = \mu\left(\nabla \vec{V} + \left(\nabla \vec{V}\right)^T\right) \tag{3-3}$$

These equations are written in the Eulerian reference frame. Since the liquid interface deforms, a method should be applied to calculate the interface. In this work the Volume of Fluid (VOF) method is used to couple the solution of flow governing equations with the calculated interface position. A piecewise linear volume tracking algorithm is applied. In order to use volume tracking method, a scalar function *f* should be defined:

$$f = \begin{cases} 1 & \textit{within the liquid phase} \\ 0 & \textit{outside of the liquid} \end{cases}$$

Since *f* is advected with the flow, the advection equation may be written as:

$$\frac{\partial f}{\partial t} + \left(\vec{V} \cdot \nabla\right) f = 0 \tag{3-4}$$

The next important step is to convert the surface tension force between the two fluids to a body force which is fed to the Navier-Stokes equation. The general boundary condition expression that should be satisfied at the interface of fluid 1 and 2 is [32]:

$$(p_1 - p_2 - \gamma\kappa)n_i = (\tilde{\tau}_{1,ik} - \tilde{\tau}_{2,ik})n_k + \frac{\partial \gamma}{\partial x_i} \tag{3-5}$$

p_1 and p_2 are the pressures on either side of the interface, n_i is a component of the unit normal $\vec{n}$ directed into fluid 1, γ is the interfacial surface tension, and κ is the local curvature:

$$\kappa = \frac{1}{R_1} + \frac{1}{R_2} \tag{3-6}$$

where R_1 and R_2 represent the principal radii of curvature. Assuming the shear stresses zero, and constant surface tension, Equation (3-5) reduces to the Laplace's equation which defines the surface tension-induced pressure jump across the liquid-gas interface:

$$\Delta p = p_l - p_g = \gamma\kappa \tag{3-7}$$

Surface tension is formulated as an equivalent volume force instead of the direct application of Equation (3-7) at the boundary condition. This approach was originally proposed in the Continuous Surface Force CSF model by Brackbill et al. [33]:

$$\vec{F}_{ST}(\vec{x}) = \gamma \int_S \kappa(\vec{y})\hat{n}(\vec{y})\delta(\vec{x} - \vec{y})dS \tag{3-8}$$

$\hat{n}$ represents a unit normal to the interface directed into the liquid. δ is the Dirac delta function and the integration is performed over area of free surface S. κ and $\vec{n}$ are geometric characteristics of the surface and may be written in terms of f:

$$\kappa = -\nabla \cdot \hat{n} \tag{3-9}$$

$$\hat{n} = \frac{\nabla f}{|\nabla f|} \tag{3-10}$$

The surface tension is now expressed as a body force and is considered in Equation (3-2) by the term $\vec{F}_b$.

3.1.2 Boundary conditions

The conservation equations, the f advection equation, and the surface tension equation are all subject to boundary conditions applied at solid interfaces, at symmetry boundaries, and at the fluid free surface. We define a unit vector $\hat{n}_\perp$ as normal to a solid boundary, and a family of unit vectors $\hat{t}_\perp$ as tangential to the boundary. The fluid velocity satisfies the usual no-slip and no-penetration conditions.

$$\vec{V} \cdot \hat{t}_\perp = 0 \tag{3-11}$$

$$\vec{V} \cdot \hat{n}_\perp = 0 \tag{3-12}$$

A zero pressure gradient is imposed across the solid boundary:

$$\nabla p \cdot \hat{n}_\perp = 0 \tag{3-13}$$

Symmetry boundaries are employed for planar symmetry to reduce the computations whenever the symmetry assumption is possible. Along the symmetry, the fluid velocity satisfies slip, no-penetration conditions:

$$\nabla\left(\vec{V} \cdot \hat{t}_\parallel\right) \cdot \hat{n}_\parallel = 0 \tag{3-14}$$

$$\vec{V} \cdot \hat{n}_\parallel = 0 \tag{3-15}$$

Across the boundary, the gradients of p and f are inherently zero:

$$\nabla p \cdot \hat{n}_\parallel = 0 \tag{3-16}$$

$$\nabla f \cdot \hat{n}_{\parallel} = 0 \tag{3-17}$$

Boundary conditions are also imposed at the fluid free surface. The zero shear stress condition is applied for velocity boundary condition:

$$\tilde{\tau}_s = 0 \tag{3-18}$$

As the surface force has already been included in the Navier-Stokes equation, the boundary condition on pressure reduces to:

$$p_s = 0 \tag{3-19}$$

To evaluate Equation (3-8) we need to define $\hat{n}$ at the contact line, where a free surface meets a solid surface. For a sessile droplet sitting on a solid substrate, $\theta = \theta_e$ is a thermodynamic property of the system at equilibrium condition. This angle is the one expressed in Equation (1-1) and is the angle between the solid-liquid and liquid-gas surface energies. The wettability of the liquid on the solid surface is also defined by this angle. Further discussion on how to apply this contact angle is presented in section 3.2.3 of this chapter.

3.1.3 Initial conditions

To initialize the droplet location and shape inside the domain, the f field is defined as a cylinder with the center placed on the desired position. At these nodes the value of f is set to one. The contact angle constraint affects the shape of the droplet after a few time steps.

3.2 Numerical technique: Flow equations

A 3D code developed by Bussmann et al. [34, 35] is used which itself is based on the RIPPLE model [36, 37]. RIPPLE is a 2D fixed-grid Eulerian code developed specifically for free surface flows with surface tension. The details of the numerical applied technique are discussed in this chapter.

Equations (3-1),(3-2),(3-4), and (3-8) are discretized on a Cartesian mesh. The Marker and Cell method, MAC, is applied in which velocities are specified at the center of cell faces while the pressure is specified at the cell center [38,39].

The discretization of f is obtained by its integration over a cell volume $\Omega_{i,j,k}$:

$$f_{i,j,k} = \frac{1}{\Omega_{i,j,k}} \int_{\Omega_{i,j,k}} f \, d\Omega \tag{3-20}$$

Cells filled with the liquid are characterized by $f_{i,j,k} = 1$, empty cells by $f_{i,j,k} = 0$ and cells partly filled by liquid (cells on interface) by $0 < f_{i,j,k} < 1$. It should be noted that the volume fraction $f_{i,j,k}$ is not a traditional scalar quantity. Where the pressure $p_{i,j,k}$ represents the value of pressure at the center of cell (i,j,k), the volume fraction $f_{i,j,k}$ is an integral quantity associated only with the volume of cell (i,j,k). It would be inappropriate to interpret $f_{i,j,k}$ as the value of f at the center of cell (i,j,k).

Equations (3-1) and (3-2) are solved with a two-step project method, in which a forward Euler timestep discretization of the momentum equation is divided into two steps:

$$\frac{\vec{V}' - \vec{V}^n}{\Delta t} = -\nabla \cdot \left(\vec{V}\vec{V}\right)^n + \frac{1}{\rho}\nabla \cdot \tilde{\tau}^n + \vec{g}^n + \frac{1}{\rho}\vec{F}_b^n \tag{3-21}$$

$$\frac{\vec{V}^{n+1} - \vec{V}'}{\Delta t} = -\frac{1}{\rho^n}\nabla p^{n+1} \tag{3-22}$$

First, an interim velocity $\vec{V}'$ is computed explicitly from convective, gravitational, and body force acceleration of the known field $\vec{V}^n$ for a time step Δt (Equation (3-21)). Next, $\vec{V}'$ is projected to a divergence-free velocity field. Combining Equations (3-22) and (3-1) at the new time level *n+1* results in a Poisson equation for pressure:

$$\nabla\cdot\left(\frac{1}{\rho^n}\nabla p^{n+1}\right)=\frac{1}{\Delta t}\cdot\vec{V}' \tag{3-23}$$

It is important that the density that appears in RHS of Equation (3-21) is the density of the incompressible liquid while in Equations (3-23) ρ^n remains in the divergence operator since there is a density change at the interface. This is designed in RIPPLE [36,37] to attain a smooth pressure distribution across cells which define the interface and are numerically characterized by $\nabla\rho\neq 0$.

The RHS of Equation (3-21) is discretized with respect to the typical convections of finite volume method [40]. The equation is integrated over the volume:

$$\frac{1}{\Delta t}\int_{\Omega_{i,j,k}}\left(\vec{V}'-\vec{V}^n\right)d\Omega=-\int_{\Omega_{i,j,k}}\nabla\cdot\left(\vec{V}\vec{V}\right)^n d\Omega+\frac{1}{\rho}\int_{\Omega_{i,j,k}}\nabla\cdot\tilde{\tau}^n\,d\Omega+\int_{\Omega_{i,j,k}}\vec{g}^n\,d\Omega+\frac{1}{\rho}\int_{\Omega_{i,j,k}}\vec{F}_b^n\,d\Omega \tag{3-24}$$

By applying Gauss' theorem, the first two volume integrals on the RHS are converted to integrals over the control volume surface $S_{i,j,k}$. We assume that the other integrants are constant through $\Omega_{i,j,k}$. Equation (3-24) becomes:

$$\frac{\vec{V}'-\vec{V}^n}{\Delta t}=-\frac{1}{\Omega_{i,j,k}}\int_{S_{i,j,k}}\vec{V}^n\left(\vec{V}^n\cdot\hat{n}_s\right)dS+\frac{1}{\rho\Omega_{i,j,k}}\int_{S_{i,j,k}}\left(\tilde{\tau}^n\cdot\hat{n}_s\right)dS+\vec{g}^n+\frac{1}{\rho}\vec{F}_b^n \tag{3-25}$$

in which $\hat{n}_s$ is unit outward normal to $S_{i,j,k}$.

Next, details of the special discretization of convective, viscous, surface tension, and pressure terms in Equations (3-21),(3-22), and (3-24) will be discussed. Also, the details on the electric field solution, including the equation discretization and the boundary conditions are discussed in the last section of this chapter.

3.2.1 Convection

The discretization of the x-momentum of the convective term of Equation (3-25) in the shaded region illustrated in Figure 3-1 is as follow:

$$-\frac{1}{\Omega_{i+\frac{1}{2},j,k}}\int_{S_{i+\frac{1}{2},j,k}} u\left(\vec{V}\cdot\hat{n}_s\right)dS = -\frac{u^{fl}_{i+1,j,k}\left\langle u\right\rangle_{i+1,j,k} - u^{fl}_{i,j,k}\left\langle u\right\rangle_{i,j,k}}{\Delta x_{i+\frac{1}{2}}} - \frac{v^{fl}_{i+\frac{1}{2},j+\frac{1}{2},k}\left\langle u\right\rangle_{i+\frac{1}{2},j+\frac{1}{2},k} - v^{fl}_{i+\frac{1}{2},j-\frac{1}{2},k}\left\langle u\right\rangle_{i+\frac{1}{2},j-\frac{1}{2},k}}{\Delta y_j}$$

$$-\frac{w^{fl}_{i+\frac{1}{2},j,k+\frac{1}{2}}\left\langle u\right\rangle_{i+\frac{1}{2},j,k+\frac{1}{2}} - w^{fl}_{i+\frac{1}{2},j,k-\frac{1}{2}}\left\langle u\right\rangle_{i+\frac{1}{2},j,k-\frac{1}{2}}}{\Delta z_k}$$

(3-26)

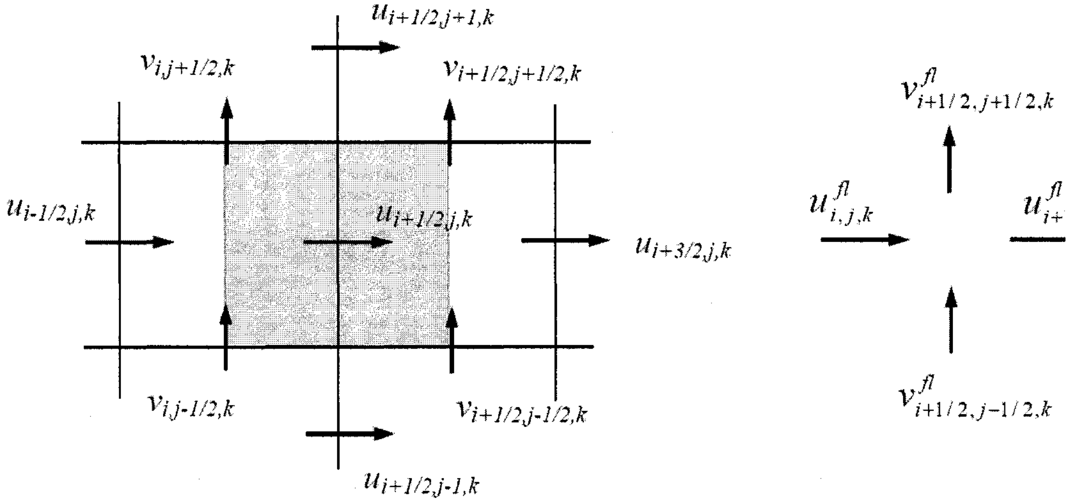

(a) (b)

Figure 3-1. (a) The shaded region is the x-momentum control volume about the velocity; (b) The interpolated flux velocities at the control volumes faces

u^{fl}, v^{fl}, and w^{fl} are the flux velocities which represent the rate of transport of the quantity $\langle u \rangle$ in or out of the control volume shown in. In our case the grid size is constant in three directions and through the whole domain. In a general form:

$$\Delta x_{i+\frac{1}{2}} = \frac{\Delta x_i + \Delta x_{i+1}}{2} \tag{3-27}$$

The same expression is valid for $\Delta y_{j+\frac{1}{2}}$ and $\Delta z_{k+\frac{1}{2}}$. By interpolating the neighboring velocities we can find the flux velocities:

$$\begin{aligned}
u^{fl}_{i,j,k} &= \frac{u_{i-\frac{1}{2},j,k} + u_{i+\frac{1}{2},j,k}}{2} \\
u^{fl}_{i+1,j,k} &= \frac{u_{i+\frac{1}{2},j,k} + u_{i+\frac{3}{2},j,k}}{2} \\
v^{fl}_{i+\frac{1}{2},j-\frac{1}{2},k} &= \frac{\Delta x_{i+1} v_{i,j-\frac{1}{2},k} + \Delta x_i v_{i+1,j-\frac{1}{2},k}}{\Delta x_i + \Delta x_{i+1}} \\
v^{fl}_{i+\frac{1}{2},j+\frac{1}{2},k} &= \frac{\Delta x_{i+1} v_{i,j+\frac{1}{2},k} + \Delta x_i v_{i+1,j+\frac{1}{2},k}}{\Delta x_i + \Delta x_{i+1}} \\
w^{fl}_{i+\frac{1}{2},j,k-\frac{1}{2}} &= \frac{\Delta x_{i+1} w_{i,j,k-\frac{1}{2}} + \Delta x_i w_{i+1,j,k-\frac{1}{2}}}{\Delta x_i + \Delta x_{i+1}} \\
w^{fl}_{i+\frac{1}{2},j,k+\frac{1}{2}} &= \frac{\Delta x_{i+1} w_{i,j,k+\frac{1}{2}} + \Delta x_i w_{i+1,j,k+\frac{1}{2}}}{\Delta x_i + \Delta x_{i+1}}
\end{aligned} \tag{3-28}$$

The flux quantity $\langle u \rangle$ can be approximated by the method of Van Leer [41] for the control volumes between two cells filled with liquid. As an example, we can write the following expression at the left edge of the control volume:

$$\langle u\rangle_{i,j,k}=\begin{cases} u_{i-\frac{1}{2},j,k}+\frac{\Delta x_i}{2}\alpha^{vL}\left(\frac{\partial u}{\partial x}\right)_{i-\frac{1}{2},j,k}\left[1-\frac{u^{fl}_{i,j,k}\Delta t}{\Delta x_i}\right] & u^{fl}_{i,j,k}>0\\ u_{i+\frac{1}{2},j,k}-\frac{\Delta x_i}{2}\alpha^{vL}\left(\frac{\partial u}{\partial x}\right)_{i+\frac{1}{2},j,k}\left[1+\frac{u^{fl}_{i,j,k}\Delta t}{\Delta x_i}\right] & u^{fl}_{i,j,k}<0\end{cases}\tag{3-29}$$

where the velocity gradients are approximated as:

$$\left(\frac{\partial u}{\partial x}\right)_{i-\frac{1}{2},j,k}=\frac{u_{i+\frac{1}{2},j,k}-u_{i-\frac{3}{2},j,k}}{\Delta x_{i-1}+\Delta x_i}$$
$$\left(\frac{\partial u}{\partial x}\right)_{i+\frac{1}{2},j,k}=\frac{u_{i+\frac{3}{2},j,k}-u_{i-\frac{1}{2},j,k}}{\Delta x_i+\Delta x_{i+1}}\tag{3-30}$$

The terms in the square brackets shift the Taylor expansions to the center of the flux volume. Further description of calculation of α and other terms are available in the same reference [41].

3.2.2 Viscosity

Expanding the viscous term in Equation (3-21) results in:

$$\nabla\cdot\tilde{\tau}=\left(\frac{\partial\tau_{xx}}{\partial x}+\frac{\partial\tau_{yx}}{\partial y}+\frac{\partial\tau_{zx}}{\partial z}\right)\hat{i}+\left(\frac{\partial\tau_{xy}}{\partial x}+\frac{\partial\tau_{yy}}{\partial y}+\frac{\partial\tau_{zy}}{\partial z}\right)\hat{j}+\left(\frac{\partial\tau_{xz}}{\partial x}+\frac{\partial\tau_{yz}}{\partial y}+\frac{\partial\tau_{zz}}{\partial z}\right)\hat{k}\tag{3-31}$$

The discretization of the $\hat{i}$ term for the control volume shown in Figure 3-2 is:

$$\left(\frac{\partial\tau_{xx}}{\partial x}+\frac{\partial\tau_{yx}}{\partial y}+\frac{\partial\tau_{zx}}{\partial z}\right)_{i+\frac{1}{2},j,k}=\frac{\tau_{xx_{i+1,j,k}}-\tau_{xx_{i,j,k}}}{\Delta x_{i+\frac{1}{2}}}+\frac{\tau_{yx_{i+\frac{1}{2},j+\frac{1}{2},k}}-\tau_{yx_{i+\frac{1}{2},j-\frac{1}{2},k}}}{\Delta y_j}+\frac{\tau_{zx_{i+\frac{1}{2},j,k+\frac{1}{2}}}-\tau_{zx_{i+\frac{1}{2},j,k-\frac{1}{2}}}}{\Delta y_k}\tag{3-32}$$

The same equations may be written for $\hat{j}$ and $\hat{k}$ terms. The individual terms of the shear stress tensor are calculated as the differences of velocity:

$$
\begin{aligned}
\tau_{xx_{i+1,j,k}} &= 2\mu \frac{u_{i+\frac{3}{2},j,k} - u_{i+\frac{1}{2},j,k}}{\Delta x_{i+1}} \\
\tau_{xx_{i,j,k}} &= 2\mu \frac{u_{i+\frac{1}{2},j,k} - u_{i-\frac{1}{2},j,k}}{\Delta x_{i}} \\
\tau_{yx_{i+\frac{1}{2},j+\frac{1}{2},k}} &= \mu\left(\frac{u_{i+\frac{1}{2},j+1,k} - u_{i+\frac{1}{2},j,k}}{\Delta y_{j+\frac{1}{2}}} + \frac{v_{i+1,j+\frac{1}{2},k} - v_{i,j+\frac{1}{2},k}}{\Delta x_{i+\frac{1}{2}}} \right) \\
\tau_{yx_{i+\frac{1}{2},j-\frac{1}{2},k}} &= \mu\left(\frac{u_{i+\frac{1}{2},j,k} - u_{i+\frac{1}{2},j-1,k}}{\Delta y_{j-\frac{1}{2}}} + \frac{v_{i+1,j-\frac{1}{2},k} - v_{i,j-\frac{1}{2},k}}{\Delta x_{i+\frac{1}{2}}} \right) \\
\tau_{zx_{i+\frac{1}{2},j,k+\frac{1}{2}}} &= \mu\left(\frac{u_{i+\frac{1}{2},j,k+1} - u_{i+\frac{1}{2},j,k}}{\Delta z_{k+\frac{1}{2}}} + \frac{w_{i+1,j,k+\frac{1}{2}} - w_{i,j,k+\frac{1}{2}}}{\Delta x_{i+\frac{1}{2}}} \right) \\
\tau_{zx_{i+\frac{1}{2},j,k-\frac{1}{2}}} &= \mu\left(\frac{u_{i+\frac{1}{2},j,k} - u_{i+\frac{1}{2},j,k-1}}{\Delta z_{k-\frac{1}{2}}} + \frac{w_{i+1,j,k-\frac{1}{2}} - w_{i,j,k-\frac{1}{2}}}{\Delta x_{i+\frac{1}{2}}} \right)
\end{aligned}
\tag{3-33}
$$

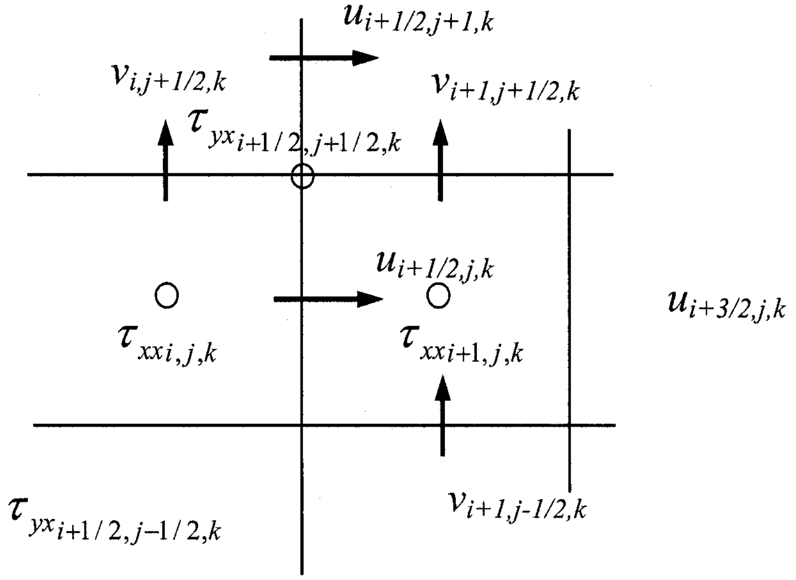

Figure 3-2. Shear stresses at the faces of an x-momentum control volume

3.2.3 Surface tension

The surface tension model used in the code comes from the Continuous Surface Tension (CSF) model [33]. Equation (3-8) needs to be discretized considering a finite approximation of δ that will convolve the surface tension force onto the fluid in the vicinity of the surface, distributed in a way that the two sides of the interface experience similar surface tension –induced acceleration.

The original discretization of Equation (3-8) results in a surface tension force distribution which induces spurious fluid motion near surfaces [33]. To reduce the spurious current a δ_ε is considered which represents a radially-symmetric kernel that is non zero with a finite radius ε. Therefore, a weighting function $w = \rho/\bar{\rho}$ is introduced in which $\bar{\rho} = (\rho_l + \rho_g)/2$. At this point it is considered that $\delta = w\delta_\varepsilon$ which results in a convolution biased towards the denser side of the interface.

$$\vec{F}_{ST}(\vec{x}) \approx \gamma \int_\Omega \kappa(\vec{y})\hat{n}(\vec{y})w(\vec{y})\delta_\varepsilon(\vec{x}-\vec{y})d\Omega \tag{3-34}$$

To discretize this equation, a local volumetric surface tension force should be calculated for each interface cell:

$$\vec{F}_{ST_{i,j,k}} = \gamma\kappa_{i,j,k}\frac{A_{i,j,k}}{\Omega_{i,j,k}}\hat{n}_{i,j,k} \tag{3-35}$$

$A_{i,j,k}$ is the free surface area in the cell and $\kappa_{i,j,k}$ and $\hat{n}_{i,j,k}$ are the cell-centered curvature and unit normal, respectively. $\vec{F}_{ST_{i,j,k}}$ is convolved to obtain a smooth force field $\vec{\vec{F}}_{ST_{i,j,k}}$:

$$\vec{\vec{F}}_{ST_{i,j,k}} = w_{i,j,k}\sum_{l,m,n}\vec{F}_{ST_{l,m,n}}\delta_\varepsilon\left(\vec{x}_{i,j,k}-\vec{y}_{l,m,n}\right)\Omega_{l,m,n} \tag{3-36}$$

where $\vec{x}_{i,j,k}$ and $\vec{y}_{l,m,n}$ are directed at cell centers. The discretization for w is:

$$w_{i,j,k} = \frac{f_{i,j,k}}{\bar{f}} \tag{3-37}$$

The average value for f is considered as $\bar{f} = 1/2$. Equation (3-36) is a summation over cells within a radius ε of $\vec{x}_{i,j,k}$. This could be applied for any mesh structure. For a uniform mesh $(\Delta x_i = \Delta y_j = \Delta z_k)$, a more precise version of Equation (3-36) is achieved by calculating the kernel contribution exactly:

$$\vec{\bar{F}}_{i,j,k} = w_{i,j,k} \sum_{l,m,n} \left(\vec{F}_{ST_{l,m,n}} \int_{\Omega_{i,j,k}} \delta_\varepsilon \left(\vec{x}_{i,j,k} - \vec{y}_{l,m,n} \right) d\Omega \right) \tag{3-38}$$

The rest is the calculation of $\hat{n}_{i,j,k}$ and $\kappa_{i,j,k}$ which reduces to the evaluation of unit normals $\hat{n}$ as $\kappa = -\nabla \cdot \hat{n}$. Further discussion on how to evaluate these values is available in [34].

To apply the contact angle constraint on the walls we calculate the surface tension force at the cells adjacent to the solid substrate. Here the contact angle constraint should be applied. This angle is a thermodynamic property of the matter and is defined by the solid-liquid and liquid-gas surface energies. The way this angle is applied in the code is by defining the direction of unit normals in the liquid cells adjacent to the solid substrate. Figure 3-3 shows the boundary cells and the contact angle. Further details are available in [34].

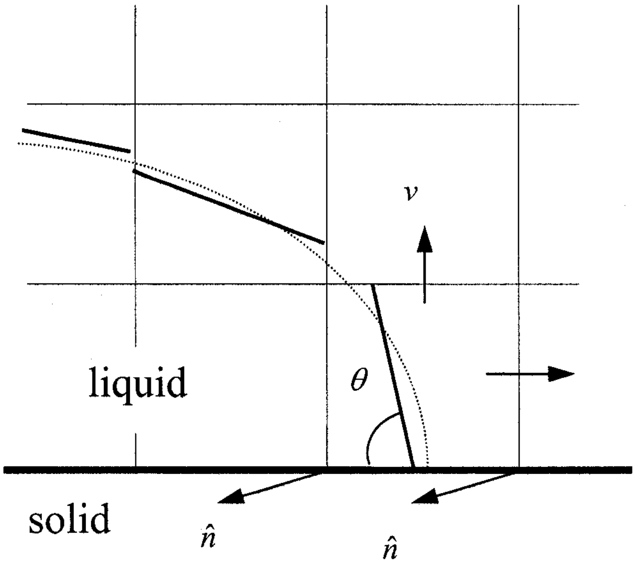

Figure 3-3. Contact angle constraint and the unit vectors defined based on that in the vicinity of a solid surface

3.2.4 Pressure

Discretization of Equation (3-23) for the pressure is the next step. The 2D representation of a seven point stencil is illustrated in Figure 3-4. To simplify the figure, the two points in z direction, $p_{i,j,k-1}$ and $p_{i,j,k+1}$, are not shown The discretization of this equation results is the following algebraic equation:

$$a_{i,j,k}p_{i,j,k}+\sum_{nb}a_{nb}p_{nb}=b_{i,j,k} \tag{3-39}$$

The index nb includes each of the six neighboring cells. Following is the definition of the coefficients:

$$
\begin{aligned}
a_{i+1,j,k} &= \frac{1}{\rho_{i+\frac{1}{2},j,k}\,\Delta x_{i+\frac{1}{2}}}\\
a_{i,j+1,k} &= \frac{1}{\rho_{i,j+\frac{1}{2},k}\,\Delta y_{j+\frac{1}{2}}}\\
a_{i,j,k+1} &= \frac{1}{\rho_{i,j,k+\frac{1}{2}}\,\Delta z_{k+\frac{1}{2}}}\\
a_{i-1,j,k} &= \frac{1}{\rho_{i-\frac{1}{2},j,k}\,\Delta x_{i-\frac{1}{2}}}\\
a_{i,j-1,k} &= \frac{1}{\rho_{i,j-\frac{1}{2},k}\,\Delta y_{j-\frac{1}{2}}}\\
a_{i,j,k-1} &= \frac{1}{\rho_{i,j,k-\frac{1}{2}}\,\Delta z_{k-\frac{1}{2}}}\\
a_{i,j,k} &= -\left(a_{i+1,j,k} + a_{i,j+1,k} + a_{i,j,k+1} + a_{i-1,j,k} + a_{i,j-1,k} + a_{i,j,k-1}\right)\\
b_{i,j,k} &= \frac{D_{i,j,k}}{\Delta t}
\end{aligned}
\tag{3-40}
$$

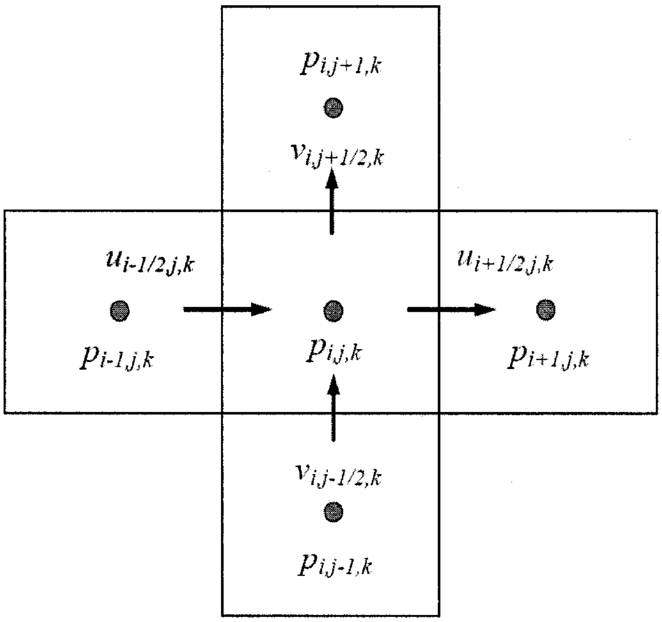

Figure 3-4. A seven point stencil for the pressure Poisson equation ($p_{i,j,k-1}$ and $p_{i,j,k+1}$ not shown)

where $D_{i,j,k}$ is the non-zero divergence of the interim velocity field

$$D_{i,j,k} = \left(\frac{u'_{i+\frac{1}{2},j,k} - u'_{i-\frac{1}{2},j,k}}{\Delta x_i} + \frac{v'_{i,j+\frac{1}{2},k} - v'_{i,j-\frac{1}{2},k}}{\Delta y_j} + \frac{w'_{i,j,k+\frac{1}{2}} - w'_{i,j,k-\frac{1}{2}}}{\Delta z_k} \right) \tag{3-41}$$

Densities at all faces are considered as the average density of two neighboring cells: for example

$$\rho_{i+\frac{1}{2},j,k} = \frac{\rho}{2}\left(f_{i,j,k} + f_{i+1,j,k}\right) \tag{3-42}$$

For void cells, the pressure equation reduces to the Dirichlet condition, $p_{i,j,k} = 0$. For fluid cells adjacent to the solid boundary, the proper coefficients are manipulated to reach the zero gradient boundary condition.

The final step is to update the interim velocity field $\vec{V}'$, based on Equation (3-24).

3.2.5 Velocity boundary conditions

At each time step, the velocity boundary conditions are imposed first following the calculation of $\vec{V}^{n+1}$ and second, following the evaluation of $f^{n+1}_{i,j,k}$. Imposing the different boundary conditions at solid surface and symmetry boundaries are achieved via the ghost cells which are a layer of cells beyond the numerical cells. Slip, no-slip, and no-penetration conditions are readily imposed. The velocity boundary conditions that are imposed at the free surface are more complicated. These may be categorized into three types: tangential velocities, new fluid velocities, and external velocities.

The first two, tangential and new fluid velocities are similar. Figure 3-5 shows a 2D example. Tangential velocities are defined at faces between two empty cells next to one or more interface cells. New fluid velocities are defined between two interface cells which were empty before the latest time step. In each case, the velocity is set equal to the nearest velocity within the fluid, reflecting zero tangential stress condition. External velocities are imposed at cell faces between an interface cell and an empty cell, attempting to reflect the zero shear stress condition while enforcing local conservation of mass. The local divergence $D_{i,j,k}$ should be zero:

$$D_{i,j,k} = \left(\frac{u_{i+\frac{1}{2},j,k} - u_{i-\frac{1}{2},j,k}}{\Delta x_i} + \frac{v_{i,j+\frac{1}{2},k} - v_{i,j-\frac{1}{2},k}}{\Delta y_j} + \frac{w_{i,j,k+\frac{1}{2}} - w_{i,j,k-\frac{1}{2}}}{\Delta z_k} \right) = 0 \tag{3-43}$$

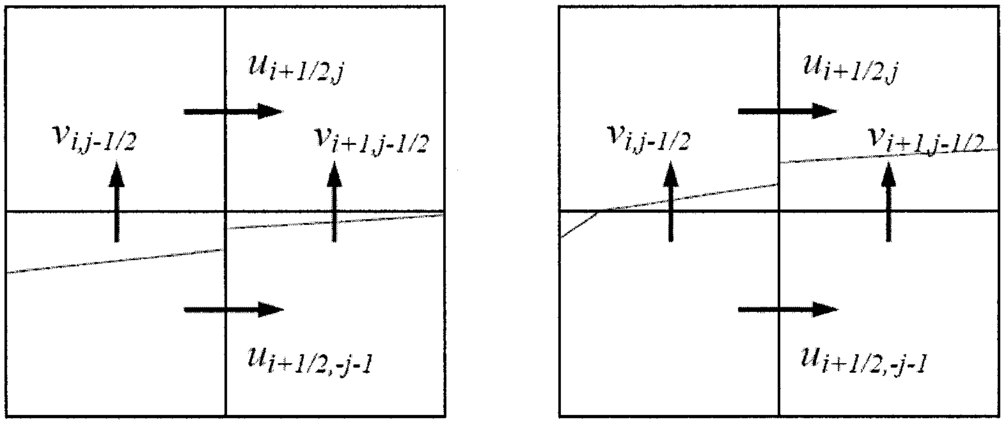

(a) **(b)**

Figure 3-5. Free surface boundary conditions in 2D: (a) tangential velocity, (b) new fluid velocity; for both cases $u_{i+\frac{1}{2},j} = u_{i+\frac{1}{2},j-1}$

3.2.6 Volume tracking

The discretization of the advection of f equation, (3-4), requires a special treatment since $f_{i,j,k}$ is in nature volumetric. The interface should be kept sharp (limited to one or two cells). Almost all the existing volume tracking schemes consist of two steps: an approximate reconstruction of the interface and then evaluation of fluxes of fluids across cell surfaces. The algorithm used in this model is that of Youngs. This method was the first one that used a piecewise linear interface calculation (PLIC) [42]. In Youngs' approach, the interface is reconstructed by locating a plane within each interface cell, corresponding exactly to $f_{i,j,k}$ and $\hat{n}_{i,j,k}$. The interface in 2D is a line crossing the cell where in 3D it becomes a 3 to 6 sided polygon depending on how the plane intersects the cell. Figure 3-6b shows the 2D volume fraction field corresponding to the exact interface of Figure 3-6a. To determine the fluid flux during each timestep, the position of the interface and the velocities at the cell faces are used. A simple illustration of volume fraction is given in Figure 3-6c.

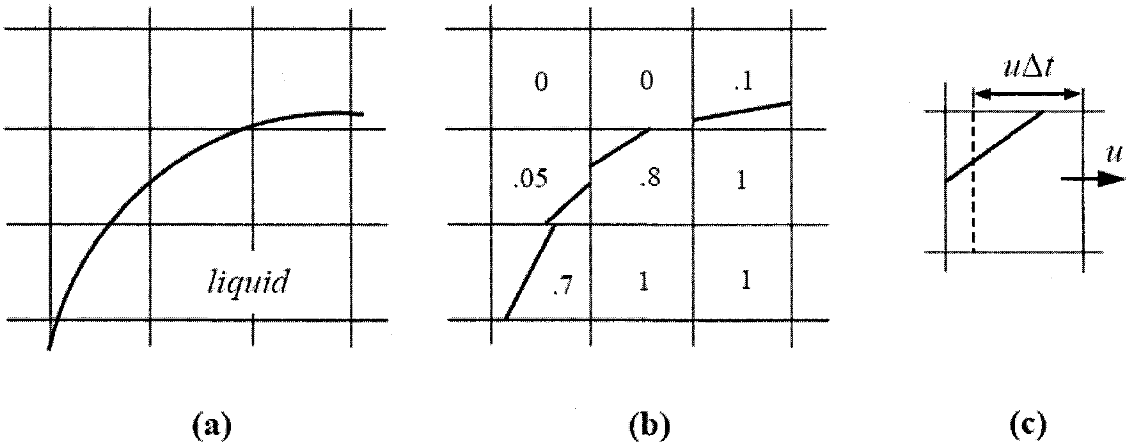

Figure 3-6.Volume fraction advection in 2D: (a) an exact liquid interface, (b) corresponding $f_{i,j}$ and the associated planar interfaces, (c) with u positive, the region to the right of the dashed line is advected into the neighboring cell.

The advection calculation begins with a reconstruction of the interface, by evaluation of a first interim field $f'_{i,j,k}$:

$$f'_{i,j,k} = \frac{f^n_{i,j,k}\Omega_{i,j,k} - \left(u^{n+1}_{i+\frac{1}{2},j,k}\langle f\rangle_{i+\frac{1}{2},j,k} - u^{n+1}_{i-\frac{1}{2},j,k}\langle f\rangle_{i-\frac{1}{2},j,k}\right)\Delta y_j \Delta z_k \Delta t}{\Omega'_{i,j,k}} \tag{3-44}$$

in which:

$$\Omega'_{i,j,k} = \Omega_{i,j,k} - \left(u_{i+\frac{1}{2},j,k} - u_{i-\frac{1}{2},j,k}\right)\Delta y_j \Delta z_k \Delta t \tag{3-45}$$

The interim field is reconstructed and the field is advected in a second direction:

$$f''_{i,j,k} = \frac{f'_{i,j,k}\Omega'_{i,j,k} - \left(v^{n+1}_{i,j+\frac{1}{2},k}\langle f\rangle_{i,j+\frac{1}{2},k} - v^{n+1}_{i,j-\frac{1}{2},k}\langle f\rangle_{i,j-\frac{1}{2},k}\right)\Delta x_i \Delta z_k \Delta t}{\Omega''_{i,j,k}} \tag{3-46}$$

where:

$$\Omega''_{i,j,k} = \Omega'_{i,j,k} - \left(v_{i,j+\frac{1}{2},k} - v_{i,j-\frac{1}{2},k}\right)\Delta x_i \Delta z_k \Delta t \tag{3-47}$$

The second interim field reconstructed at the next step, followed by the evaluation of $f^{n+1}_{i,j,k}$:

$$f^{n+1}_{i,j,k} = \frac{f''_{i,j,k}\Omega''_{i,j,k} - \left(w^{n+1}_{i,j,k+\frac{1}{2}}\langle f\rangle_{i,j,k+\frac{1}{2}} - w^{n+1}_{i,j,k-\frac{1}{2}}\langle f\rangle_{i,j,k-\frac{1}{2}}\right)\Delta x_i \Delta y_j \Delta t}{\Omega_{i,j,k}} \tag{3-48}$$

The $\langle f\rangle$ refers to the volume fractions of the *flux volume*. So they are not equal to the volume fractions of donor cell unless the cell is full or empty or the interface lies parallel to the flux direction.

3.2.7 Timestep restrictions

There are some restrictions on the magnitude of the allowable timestep to maintain the stability of the solution. These restrictions are imposed by the explicit evaluation of the convective, viscous, and surface tension terms. Momentum cannot be advected more than a single cell, implying that the Courant number should be less than the following value:

$$\max\left[\frac{|u_{i,j,k}|\Delta t}{\Delta x_i},\frac{|v_{i,j,k}|\Delta t}{\Delta y_j},\frac{|w_{i,j,k}|\Delta t}{\Delta z_k}\right]<1 \tag{3-49}$$

As fluid volume can only be advected into neighboring cells, this condition is required by the volume tracking algorithm as well.

In the same way, momentum cannot diffuse more than one cell in a single timestep:

$$\Delta t<\frac{\rho}{\mu}\cdot\min\left[\frac{(\Delta x_i)^2(\Delta y_j)^2}{(\Delta x_i)^2+(\Delta y_j)^2},\frac{(\Delta x_i)^2(\Delta z_k)^2}{(\Delta x_i)^2+(\Delta z_k)^2},\frac{(\Delta z_k)^2(\Delta y_j)^2}{(\Delta z_k)^2+(\Delta y_j)^2}\right] \tag{3-50}$$

And finally, the timestep should be small enough to resolve the propagation of capillary waves that cannot be allowed to travel more than a cell width. The following relation was derived by Brackbill et al. [33].

$$\Delta t<\sqrt{\frac{\rho}{4\pi\gamma}}\cdot\min\left[(\Delta x_i)^{\frac{3}{2}},(\Delta y_j)^{\frac{3}{2}},(\Delta z_k)^{\frac{3}{2}}\right] \tag{3-51}$$

The time step for any time level then is the minimum value allowed by any of these criteria.

3.3 Numerical technique: Electric potential

In this section, the electric potential equation derived in Chapter 2 is discretized. The main contribution of the current study in the numerical algorithm is adding the electric field equation to the flow equation and solving them simultaneously to capture the effects of the imposed electric field at each timestep throughout the computational domain. Laplace's equation (2-9) is solved at the beginning of each timestep, with a finite difference approach. Here an approach with second order accuracy has been chosen. The discretized version of Equation (2-9) in space is:

$$\psi_{i,j,k} = \frac{1}{6}\left[\psi_{i+1,j,k} + \psi_{i-1,j,k} + \psi_{i,j+1,k} + \psi_{i,j-1,k} + \psi_{i,j,k+1} + \psi_{i,j,k-1}\right] \tag{3-52}$$

The electric potential ψ is calculated at each node *i,j,k*. Equation (3-52) is solved with an iterative method with the precision of 10^{-6} V. Having known the value of the electric potential at each node the Young-Lippman's equation, (2-3), is applied in a discretized form to calculate the surface energy change due to the applied voltage:

$$\theta_{i,j,k}^{new} = \cos^{-1}\left[\cos\theta_0 + \frac{\varepsilon_0\varepsilon}{2d\gamma_{LG}}\left(\tilde{\psi}_{i,j,k}^{n}\right)^2\right] \tag{3-53}$$

Subsequently, the newly calculated values for the contact angle at each grid, are imposed as contact angle constraints on the solid-liquid interface. Figure 3-7 shows two different cases. In case (a), there is no electric potential present in the domain, while in case (b) the values of the electric potential calculated throughout the domain is shown with $\psi_{i,j,k}$. The value of the electric potential used in Equation (3-52) should be calculated. Since the electric potential for the cells partly filled with liquid is considered zero in the boundary conditions, its value is replaced by the average value of the next two empty cells:

$$\tilde{\psi}_{i,j,k} = (\psi_{i+1,j,k} + \psi_{i+2,j,k})/2$$

As it may be seen, the contact angle has decreased in case (b) due to the existence of the electric potential on the nodes. This yields a change in the direction of the normals which then affects the value of the surface tension force calculated with CSF model discussed in Section 3.2.3.

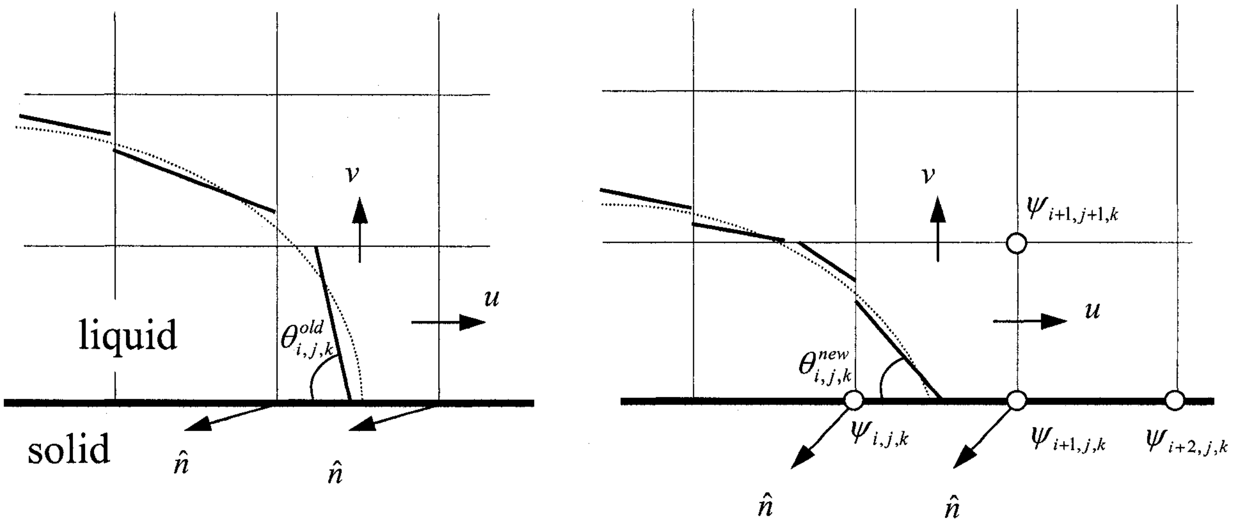

(a) (b)

Figure 3-7. Contact angle constraint and the unit vectors defined (a) before applying the voltage; (b) after applying the voltage

3.3.1 Electrical boundary conditions

The electric field pattern through the domain is variable with time and space. There are two main reasons for such behaviour. First, the electrodes are switched on and off sequentially and second, the droplet position in the domain changes the electric field. The top electrode is grounded and the conductive droplet is in contact with this electrode. Thus, the droplet potential is considered zero. The moving droplet imposes a zero potential moving boundary condition. To apply this boundary condition, the electric potential of the cells with the values of $f \neq 0$ (where there is liquid) is assigned to zero. The powered electrode location is also defined. This location changes when the electrode is switched. A schematic of the computational domain with the required electrical boundary conditions is shown in Figure 3-8.

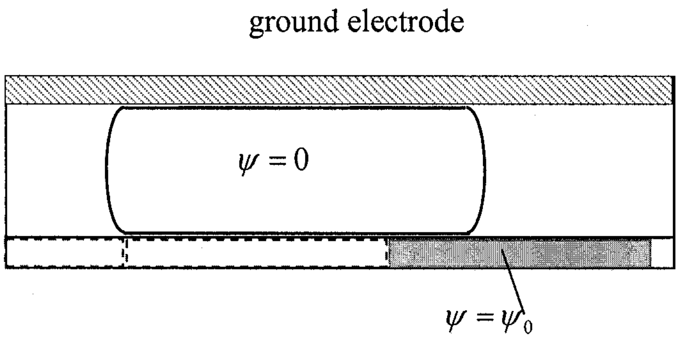

Figure 3-8. The electrical boundary conditions, the powered electrode is shown darker

The following flow chart shows the complete numerical algorithm employed to solve the problem.

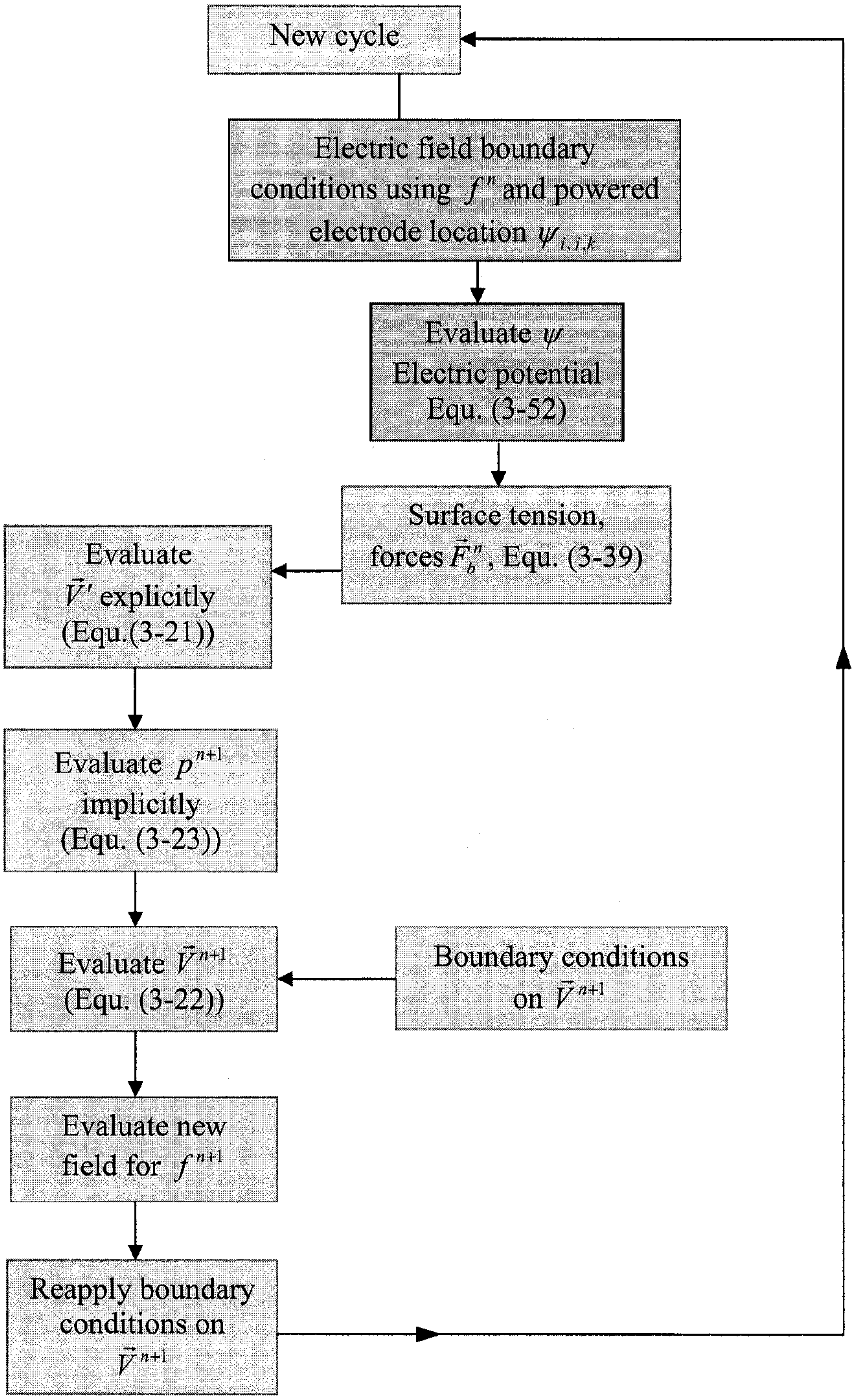

Figure 3-9. The numerical algorithm applied in this study

3.4 Geometry

The geometry used in the following simulations (shown in Figure 3-10) is the same as the one used in the experiments performed by Pollack et al [19]. The droplet diameter is 1900 μm. At the beginning, the droplet is defined to be cylindrical between the channel top and bottom plates. The equilibrium contact angle of 104° is considered for the non-actuated condition, where the droplet sits on a Teflon-covered plate.

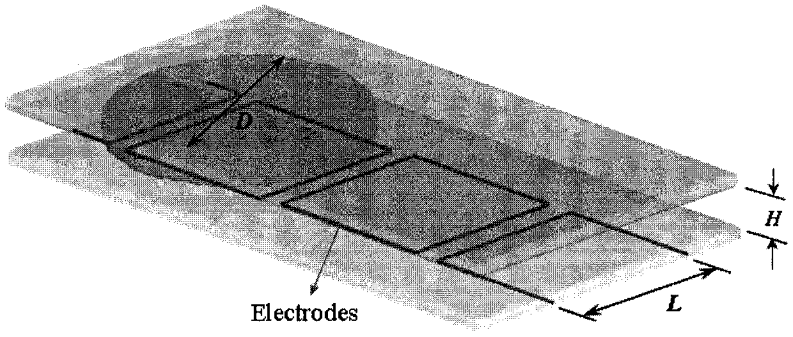

Figure 3-10. Model geometry in 3D

The channel gap, H, is set to 300 μm which is constant for all the simulations. The electrodes are squares with a dimension of L=1500 μm unless stated. The size of the grid is set to 50 μm. In the experiments performed by Pollack et al., interdigitated electrodes were used. These are the electrodes that have the zigzag configuration minimizing the separation distance between the two adjacent electrodes in the absence of electrical connection. Such electrodes are illustrated in Figure 3-11. To achieve the same pattern in the numerical simulations, the spacing between the two adjacent electrodes is set to zero. The insulator layer thickness is set to 900 nm. The insulator is Parylene C with the permittivity of $3\varepsilon_0$. A plane of symmetry can be identified; therefore, symmetry boundary condition is applied and only half of the domain is solved.

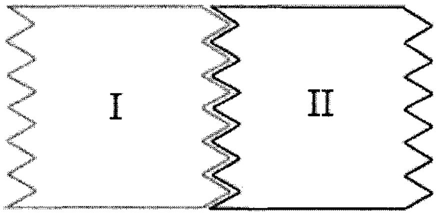

Figure 3-11. Schematic of two interdigitated electrodes

4. Results and Discussion

In this chapter, the results of the numerically solved equations with the proper boundary conditions are presented. This work mainly focuses on the droplet actuation and droplet transport in microchannels. The onset of actuation procedure and its effects on the droplet deformation and motion are investigated. In addition, the droplet velocity and the effects of different switching frequencies and electrode sizes on droplet actuation are studied.

The Laplace's equation governing the electric potential, with the required boundary conditions is solved. A channel gap of 600 μm is chosen to show the electric potential distribution and the f field representing the droplet. Symmetry boundary condition is imposed at the center plane to reduce the computational time. The actuation voltage of 55V is applied. A typical solution of the electrohydrodynamic equations is shown in Figure 4-1. This figure shows the interaction between the droplet and the electric field. The droplet is located at the left side of the electrode while the powered electrode is seen after the droplet. The two other electrodes are also illustrated. These two electrodes are not powered at this step. The equipotential surfaces at the right side of the droplet are shown along the channel gap. The existence of the electric potential at this section leads to the change in surface energy. The energy imbalance between the droplet leading and trailing edges then, induce the motion of the droplet toward right. There are basically two sorts of electrowetting forces acting on the droplet: first is the force on the liquid-gas interface, second, is the force on the tri-phase contact line. The first force is due to the presence of the charges at the interface and is directly proportional to the ratio of dielectric thickness to the channel gap as is shown in Equation (a - 12). In cases where the dielectric thickness is much smaller than the channel gap, like the cases studied here, the value of this force is negligible. The second force is important and plays an essential role in the droplet actuation. This latter force is due to the existence of the free charges at the tri-phase contact line. The tri-phase contact line is the line where the three interfaces of solid-liquid, liquid-gas, and solid-gas meet. The electric potential distribution on this line leads to a variable electric force field on this region that stretches the droplet and changes the energy distribution in the region.

A closer view of the tri-phase contact line is shown in Figure 4-2. The potential variation is also shown. As it may be observed, the tri-phase contact line which is affected by the electric field is smaller when the electrode width is smaller. This also affects the droplet deformation. In case (b) the deformation is rather local, near the affected tri-phase contact line while in case (a) with the electrode size twice the case (b) the whole droplet has deformed to an oval shape.

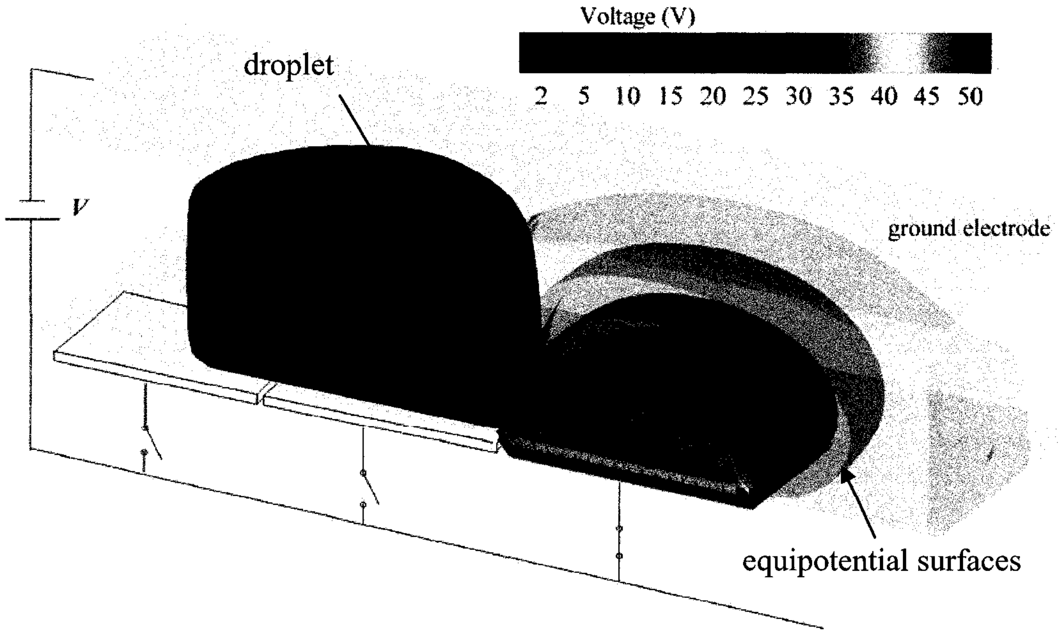

Figure 4-1. The electric potential pattern inside the channel; the powered electrode is shown in red (only half of the domain is shown.)

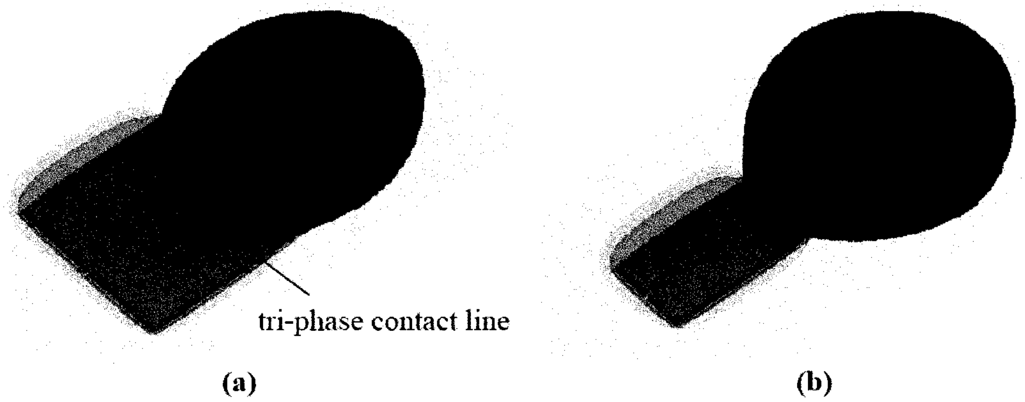

(a) (b)

Figure 4-2. A closer view of the tri-phase contact line and the potential variation on it, the electrode width in case (a) is twice as case (b)

4.1 Droplet actuation

After calculating the electric field that surrounds the droplet, its effect on the droplet should be studied. Two different aspects are investigated; 1) the droplet morphology while approaching the electrode and advancing on it, 2) the droplet deformation while traveling on a series of electrodes along the channel.

4.1.1 Onset of actuation

In Figure 4-3 different steps of droplet actuation are shown. The droplet is primarily at rest and there is no actuation force. Then, the electrode located at the separation distance of 300 μm from the droplet leading edge is switched on. The objective is to see how the droplet is actuated and deformed while approaching the powered electrode. In the graphs, the contact angles formed between the droplet and the bottom plate, θ, are plotted for various polar angles, α. The symmetry boundary condition is used to simulate the droplet. Hence, only half of the domain is modeled. The contact angles shown in Figure 4-3 are for the modeled half (the upper section of the center line). The other half is only a mirror image and is not shown in the line graphs.

As it may be observed, for an actuation voltage of 55 V, when the separation distance is 200 μm, there is no contact angle change due to the actuation. The contact angle remains 104° for all grid points (Figure 4-3a). In Figure 4-3b, the distance is 150 μm and a portion of up to the polar angle of 24° is influenced by the electric field. In case (c), the droplet touches the electrode with an actuated portion of $\alpha = 28°$ and the contact angle, θ, reduces significantly to 63°, while its value is 93° for case (b).

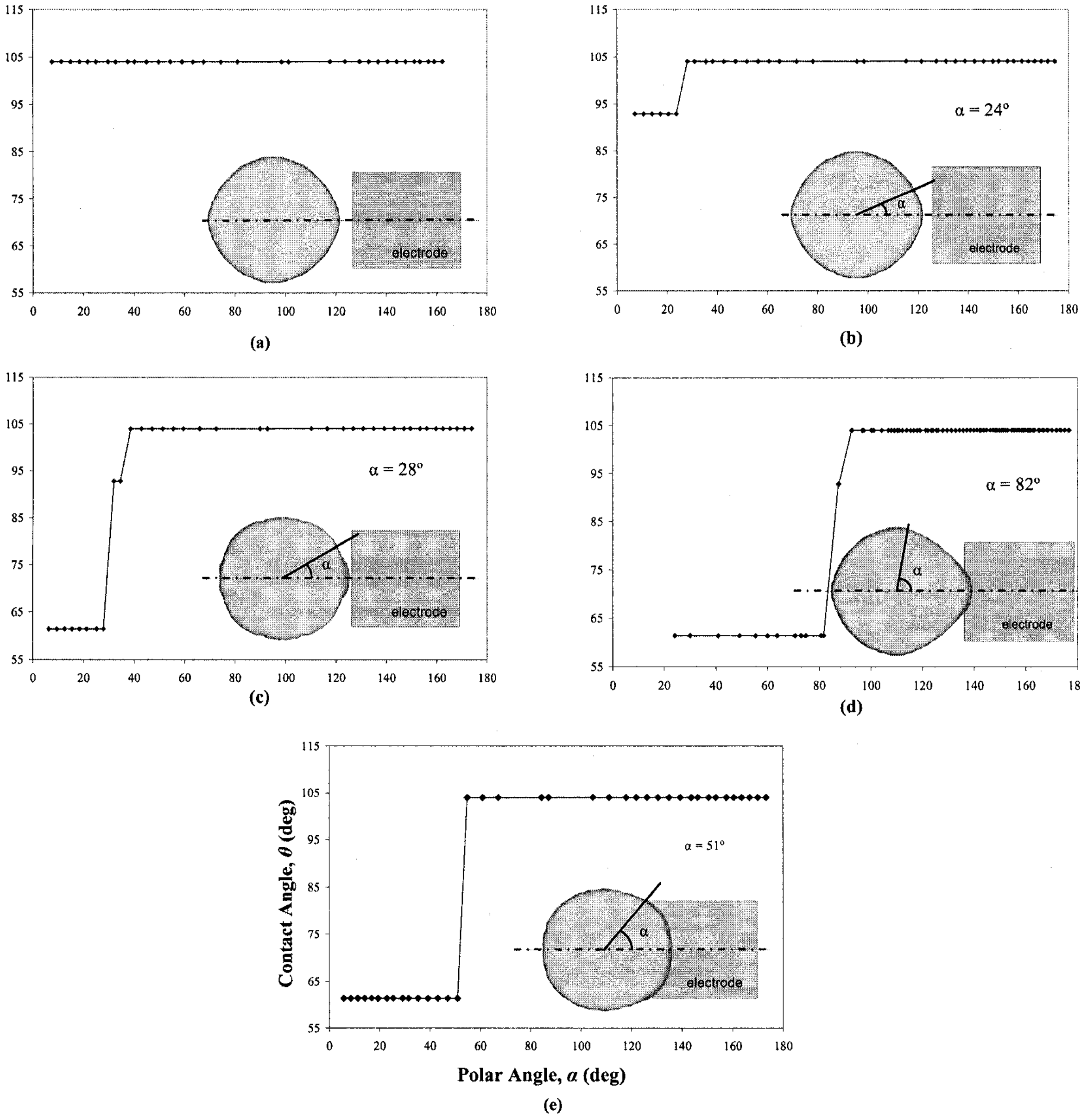

(a) (b) (c) (d) (e)

Figure 4-3. Droplet actuation process while approaching to the electrode: (a) 200 μm and (b) 100 μm (c) 50 μm separation of droplet leading edge with the powered electrode; while on the electrode (d) 50 μm and (e) droplet 300 μm

The actuated portion increases until we reach to the point that the droplet touches the electrode edge. For the next two cases (d) and (e) the droplet is on the electrode. Case (d) is an instant after touching the electrode and in case (e), the droplet has advanced about 300 μm on the electrode. In case (d), the droplet advancement on the electrode is only 50 μm and it encounters the maximum actuated portion which is 82° which is also larger than when the droplet is completely covering the length of the electrode (Figure 4-3e). That is because when the conductive droplet sits on the electrode, the electric potential pattern around the contact line undergoes an acute change from the electrode potential to zero.

In the case of Figure 4-3e only the portion of the tri-phase contact line that is on the electrode is actuated while in Figure 4-3d a large portion before the electrode is also affected. Any further advancement of the droplet on the electrode results in the same actuated area represented in Figure 4-3e. Since a larger portion of the contact line is actuated for an approaching droplet (as shown in Figure 4-3d), one may conclude that an array of electrodes with smaller length would better actuate the droplet. In such a case, a small portion of the droplet is placed on the electrode and the influence of the electric potential is present in a larger portion of the leading edge.

The electrodes with smaller lengths are believed to have a better performance as the backward effect of the electrowetting force decreases. The electric force is a radial force on the droplet periphery, oriented outward from the droplet. The existence of the electric field at the regions other than the leading edge results in the outward forces in that region. These forces are not favorable when their resultant is not in the direction of droplet motion. In the case that they exist at the tailing half of the droplet, a resultant backward force is exerted to the droplet that reduces its velocity. This also shows that the smaller lengths help preventing from such unfavorable effects. However, such electrodes are difficult to be fabricated.

As it has been discussed before, once the droplet touches the electrode, the contact angle distribution changes along the tri-phase contact line. The consequence is the droplet stretching on the electrode. Figure 4-4 shows both the top and side views for two different timesteps: first at the onset actuation (Figure 4-4a), and then after 600 μs when the droplet leading edge reaches almost half of the electrode (Figure 4-4b). In the first case, the droplet has a circular shape which shows that the electrowetting force has not deformed the droplet yet. As time passes and the electrowetting force influence appears, the contact line will be drawn toward right and as a result, the droplet stretches on the solid surface. In case (b), the droplet has achieved an oval shape. This means that the droplet diameter in the direction of motion increases, while, to conserve the mass, the diameter decreases in the direction perpendicular to the motion. The increase in diameter is also obvious in the side views.

Figure 4-5 shows the actuation process at various times on the first electrode. It can be seen that the contact angle at the leading edge (right end) is smaller than the one at the trailing edge (left end). The results are shown for different times after starting the actuation. At 700 μs the droplet leading edge passes almost half of the electrode. The changes in electric potential pattern by advancement of the droplet on the electrode are obvious. In addition, the droplet elongation in the direction of motion may be observed. The droplet behaves differently while moving on a series of electrodes along the channel. This is discussed in the next section.

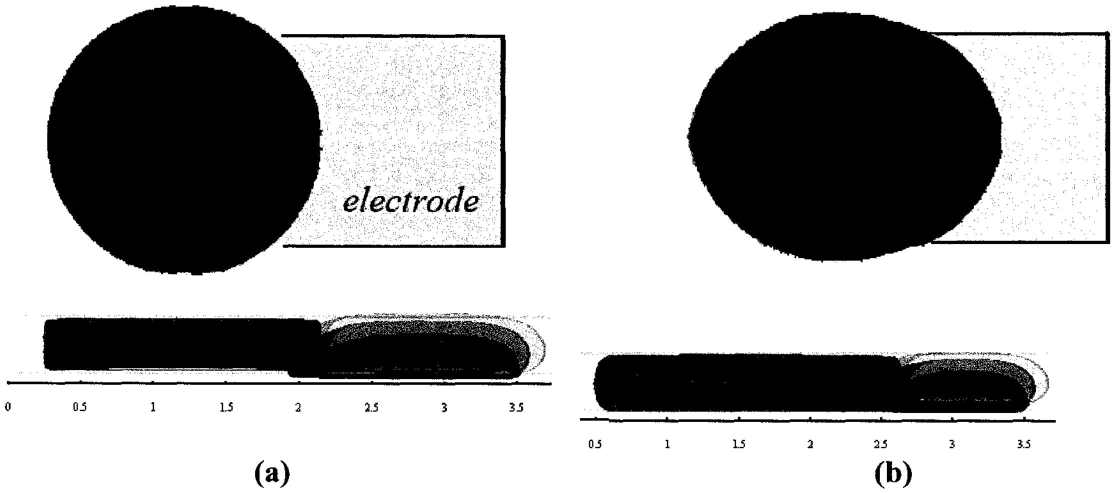

Figure 4-4. Top and side views of the droplet: (a) just at the beginning of actuation, (b) after a short time

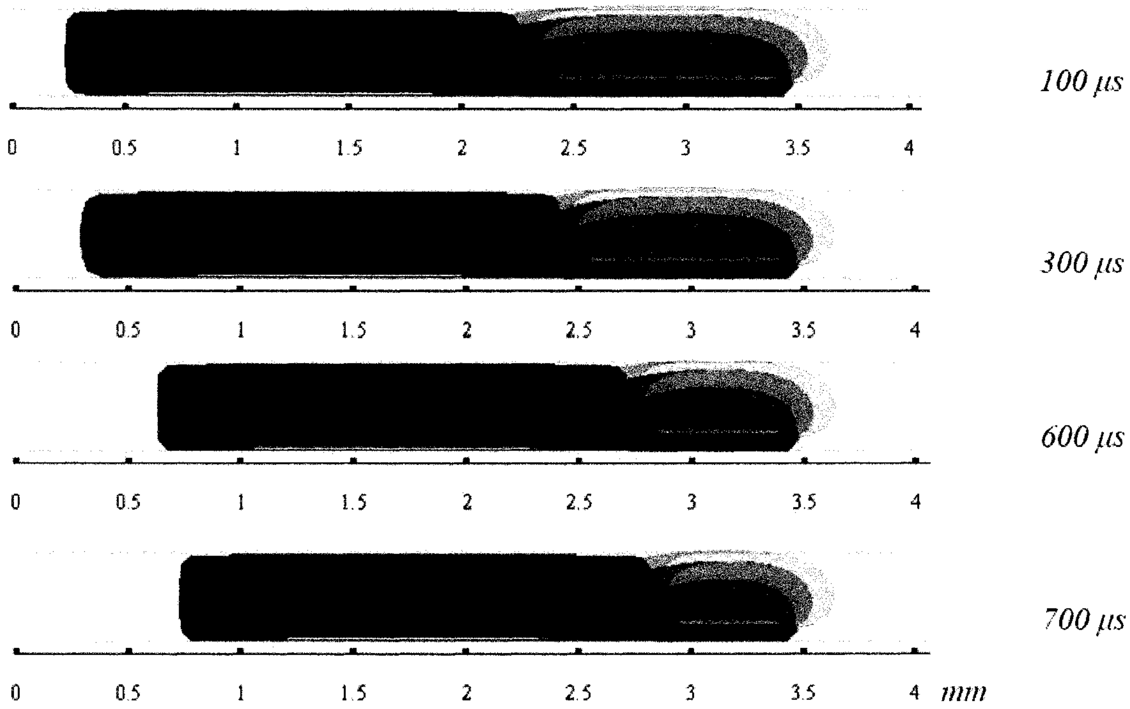

Figure 4-5. Droplet advancement on the first electrode at different times

4.1.2 Actuation over a series of electrodes

The droplet is still accelerating while it travels on the first and even second electrode. Further on, the affected portion of the contact line is different along the channel. Figure 4-6 shows the droplet at the beginning of the first four electrodes. It is observed that the oval shape is remarkable for the third and forth electrodes and the droplet stretches more in the direction of motion than in the other directions. In addition, by reaching to an almost steady state velocity, the droplet deformation reduces. At this stage, the overall behavior of the droplet remains almost constant while it faces bounded instantaneous changes.

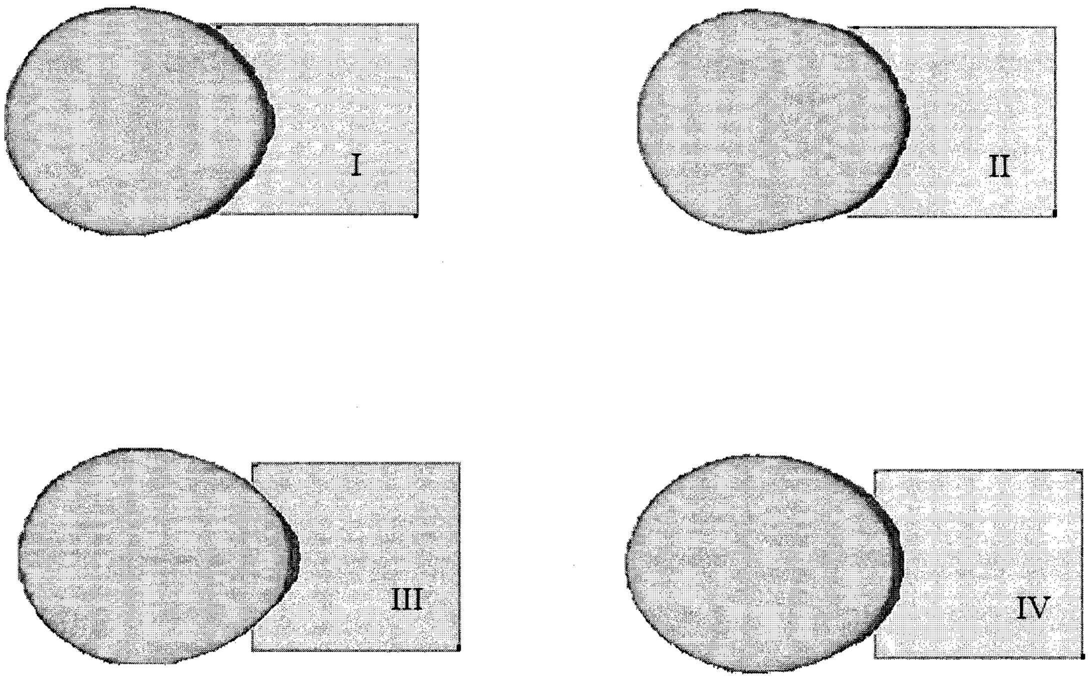

Figure 4-6. Droplet morphology when traveling along different consecutive electrodes; the electrode number is indicated by latin numbers in each case.

4.2 Droplet Velocity

Droplet velocity is important in microfluidic devices responsible for delivering liquids. In this section, droplet velocity is discussed and the validation of numerical results against the experimental data in the literature is presented.

The droplet motion induced by electrowetting is a very complex phenomenon in nature. As it is shown in the last section, this motion is a combination of deformation and transportation. The force source is variable both in time and space meaning that in the domain, there exist variable forces in each point at the interface. Observations show that the droplet stretches in the direction of motion while its diameter decreases in the direction perpendicular to the motion. The contact line moves with a variable velocity. (Figure 4-7) shows the instantaneous velocity of the leading edge versus droplet location.

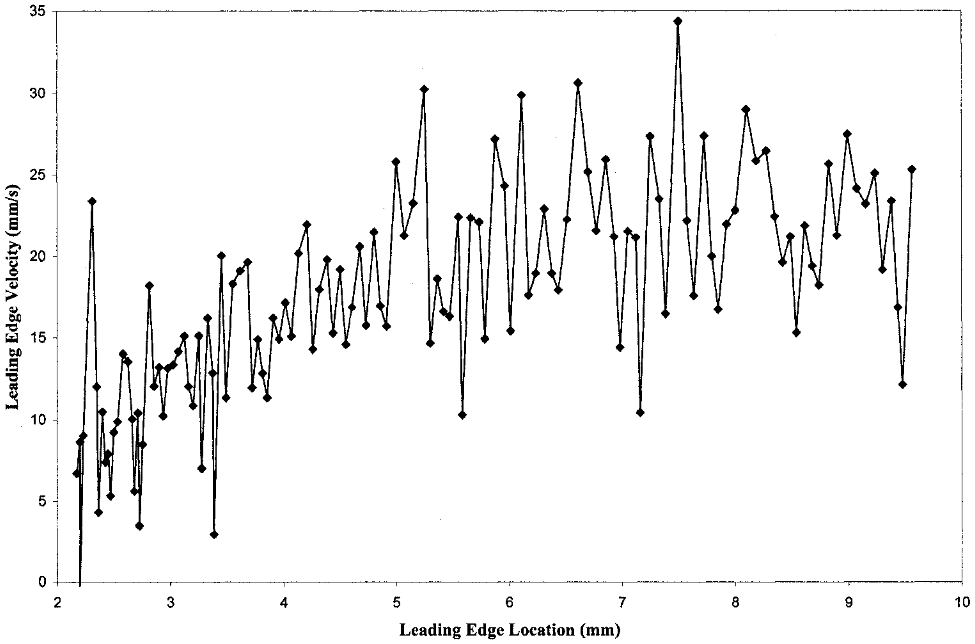

Figure 4-7. Droplet instantaneous velocity

In order to be able to study the droplet velocity, the average velocity should be defined. For the cases where the droplet steady state velocity in the domain is studied, the velocity of droplet leading edge is calculated by knowing the location and the time of two arbitrary points along the channel. The two points should be far enough from the starting position since we need to exclude the effects of the acceleration at the beginning of the motion. Also these points should be far from each other so that the instantaneous oscillations do not appear in the resulting velocity. Based on this study, depending on the actuation voltage (less than 60V), the droplet reaches to a quasi steady state condition after reaching the second or third electrode. This will be discussed and studied in detail on graphs in the next section. Each pair of points (with the distance of at least one electrode length) in this region should result in a unique velocity. In this case, the velocity based on the droplet leading edge displacement along more than two electrodes is calculated.

Figure 4-8 shows the droplet leading and trailing edge velocity. According to the leading edge curve, the droplet accelerates until it reaches a steady state condition. The trailing edge velocity is also shown in this figure. It may be observed that the trailing edge accelerates and decelerates continuously. For the rest of this work, the velocity of the leading edge is chosen since the leading edge has a more stable behaviour and its velocity pattern is easier to study.

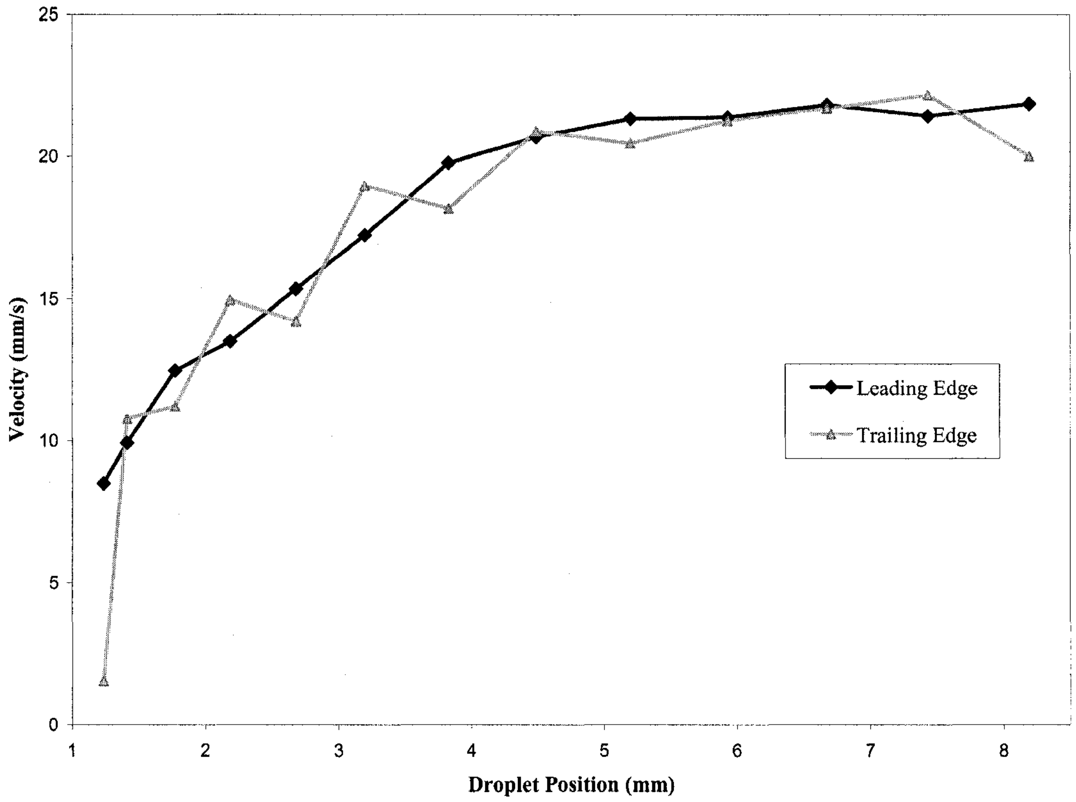

Figure 4-8. Droplet velocity change through the channel; both leading and trailing edge velocities are shown.

Obviously, the droplet velocity is proportional to the applied actuation voltage. Higher actuation voltages result in larger velocities. Figure 4-9 shows the numerically obtained results by varying the actuation voltage from 35V to 60V. The experimental data are also provided from [19] to compare with the simulation results. A threshold voltage always exists, below which the droplet does not start moving. When a droplet advances on a surface, it has a contact angle which is different from when it recedes. This difference is known as the contact angle hysteresis. As reported by Pollack et al. [19,20], for a system of water as liquid and air as the surrounding medium, this voltage is about 47V. By increasing the voltage from zero, the droplet starts to deform. The contact angle changes from the non-actuated equilibrium value of 104° to smaller ones. This means that the droplet stretches on the plate while staying at the same position. Before any forward movement, it has to overcome some restrictions, such as the viscous forces and the contact angle hysteresis. The advent of actuation was studied in detail in Section 4.1. In those simulations, no model for contact angle hysteresis is considered. In effect, primarily, the droplet started to move in a voltage of 30V. This threshold is due to the existence of the viscous forces between the liquid and the solid wall.

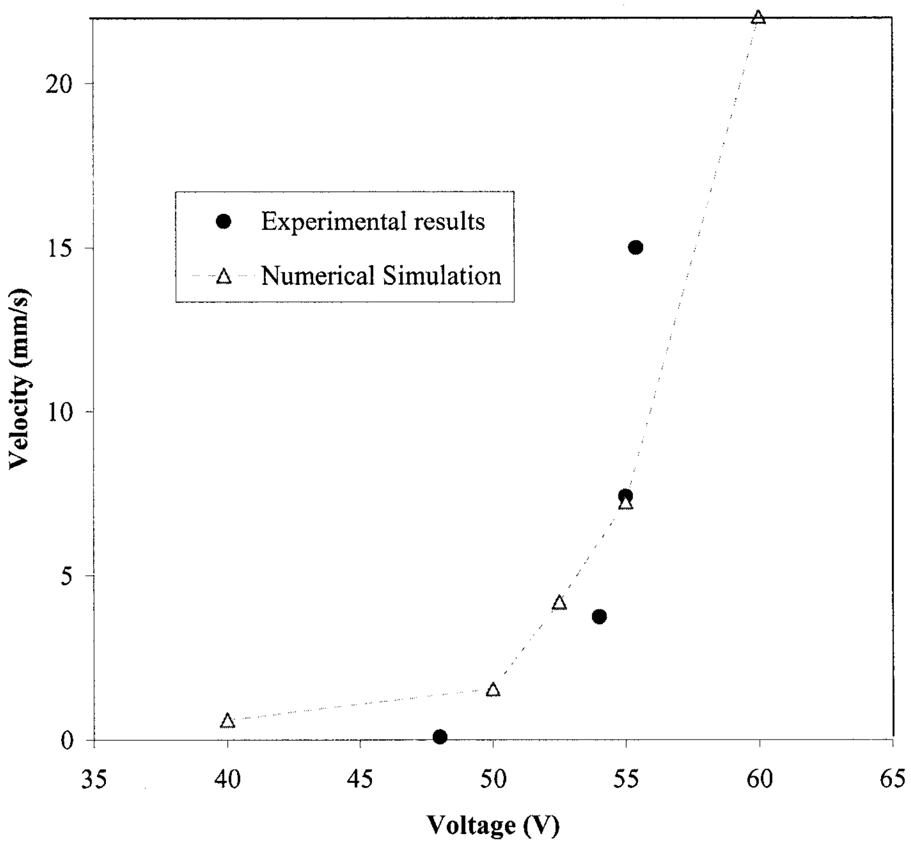

Figure 4-9. Droplet velocity comparison between the numerical results and the experimental data of Pollack et al. [19]

To consider the effect of the contact angle hysteresis, which has been neglected in the simulation, the numerical curve has been shifted to a value of 5V to right. This allows including this effect with a simple shifting into the current model. This assumption for the contact angle hysteresis effect is fairly satisfying. The numerical curve and the experimental results are almost in the same range. However, the slope in the numerical curve differs slightly from the experimental one. This is believed to be due to the assumption of a constant contact angle hysteresis for all the cases.

It should be noted that the origins of the contact angle hysteresis is not still well-understood. Only few empirical models for very specific problems exist. Pollack et al. [19,20] explain the source of this threshold voltage as the difference between the leading and training edge equilibrium contact angles. It means that the equilibrium contact angles between a particular liquid-solid pair are not unique, and vary over a finite range. Several studies were performed to investigate the source of the contact angle hysteresis and the resulting delay in movement of the droplet. They indicated that surface roughness and surface heterogeneity (both physical and chemical) are related to this phenomenon [9,10]. What is known is that the hysteresis is a highly case-dependant phenomenon which means even for a same configuration, e.g. Teflon, water, and air, it depends on the surface characteristics, which can come from the preparation procedure.

To reduce the effect of the hysteresis, the surrounding medium can be changed. Pollack et al. [19,20] performed experiments with silicone oil as the surrounding medium. In fact, they studied most of their cases with silicone oil rather than air. It is more favorable as the droplet evaporates faster in the air and also the threshold voltage decreases with silicone oil, to a value of about 20V (27V less than air). To do experiments with the silicone oil, first the channel is filled with oil. Then the water drop is dispensed between the two plates in the oil. By this way, there will be a very thin layer of silicone oil between the droplet and the plates which decreases the threshold voltage. When a voltage is applied, the silicone oil layer between the drop and the substrate disappears after a while and the droplet will be in direct contact with the substrate and starts moving. As it can be noticed, this complex phenomenon requires a two-fluid tracking model. For this reason, in this work, all the simulations are done considering air as the surrounding medium.

From Figure 4-9, one can see that in the range of 50-60V, the values of the droplet velocity for both numerical and experimental data are close. Hence, all further studies are performed with the same actuation voltage range in order to have more realistic prediction of droplet behaviour.

4.3 Grid dependency test

In order to do the simulations, one needs to define the grid size to discretize the domain. As it has been mentioned in Section 3.2.3, to achieve more accurate results, the grids should be cubes, means that their sizes in all directions should be the same. A fine grid is needed to capture the channel height of 300 μm while due to the model restriction, the same grid size is needed along the channel length which is 1cm. This increases the total number of grids in the computational domain. In this study, two different grid sizes are applied and the results are shown in Figure 4-10. The first case consists of 38 grids per droplet diameter (50 μm grid size), while this increases to 76 grids per diameter for the second case (25 μm grid size) .The number of grids in the second case is 8 times more than the first one. Farther decrease in the grid size leads to a very long computational time and needs much bigger memory size. Due to the consistency of the results for both cases, the 38 grids per diameter case is used in the current work.

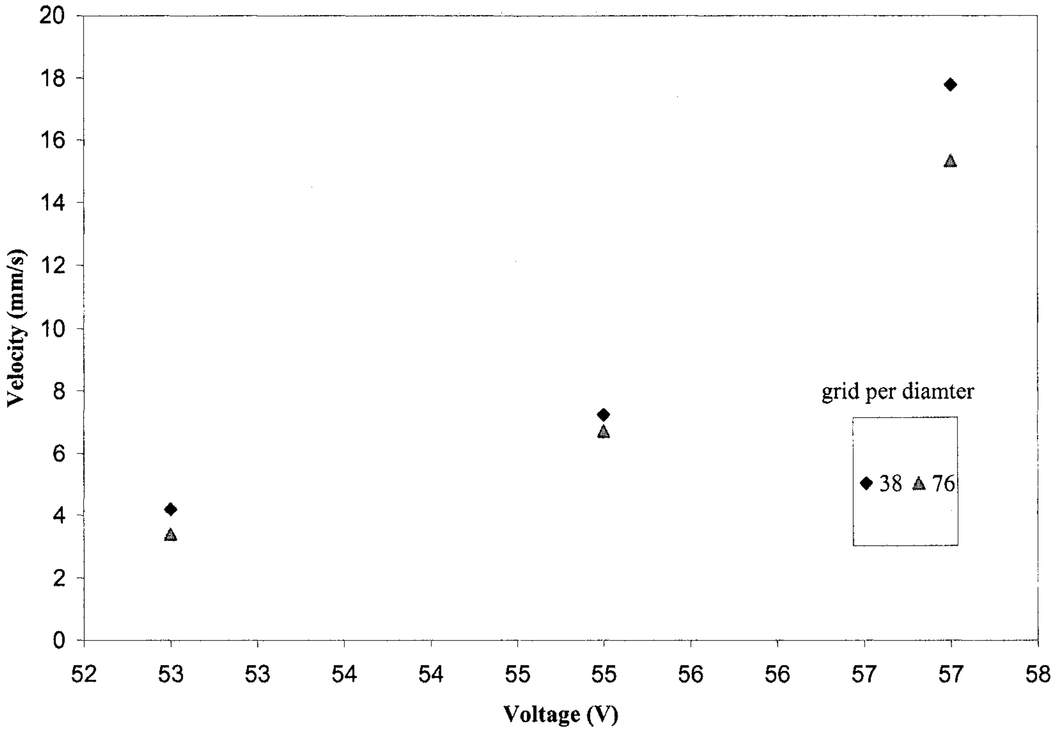

Figure 4-10. Grid dependency test results

4.4 Electrode switching frequency

An important issue in handling the electrowetting-based actuated devices that are used to transfer the droplet through microchannels is the electrode switching time. It would be ideal to turn on the next electrode at the exact moment that the droplet leading edge reaches to the end of the current powered electrode. This is the perfect case, based on that the previously presented results have been obtained. However, while performing experiments, it would be very difficult to control the system with this ideal switching time. The first step is to determine the value of this time interval, and second is to know how various switching times would influence the droplet motion. Since experiments in that scales with such devices is both expensive and challenging, the numerical study is performed to predict the droplet behaviour and hence, make it possible to choose the required time intervals for further experimental investigations.

In order to proceed, the definition of *electrode switching frequency* should be explained. This frequency is the inverse of the required time that the droplet leading edge needs to travel from the beginning to the end of a single electrode. As it is known, the droplet velocity over the first few electrodes is variable; as a result this frequency is variable too. Hence, what is considered as the frequency is the one that is obtained when the droplet reaches to the quasi steady state condition. Therefore, the droplet average velocity may be expressed as:

$$V = F \cdot L \tag{4-1}$$

where L is the electrode length and F is the switching frequency.

Figure 4-11 shows the effect of different electrode switching frequencies on the droplet motion and velocity through the channel. The actuation voltage is set to 60V while the droplet switching frequency is varied to the values both higher and lower than the ideal case. This case is highlighted with a bold black curve with the steady state switching frequency of 14.3 Hz. As it may be seen, the droplet accelerates within the first two electrodes and reaches to a plateau region in which the average velocity change is negligible representing the steady state section. The steady velocity is achieved only in the ideal case. This velocity is about 22 mm/s. For all other cases, the velocities fluctuate which means they remain in a certain range, or drops to zero depending on the input frequency.

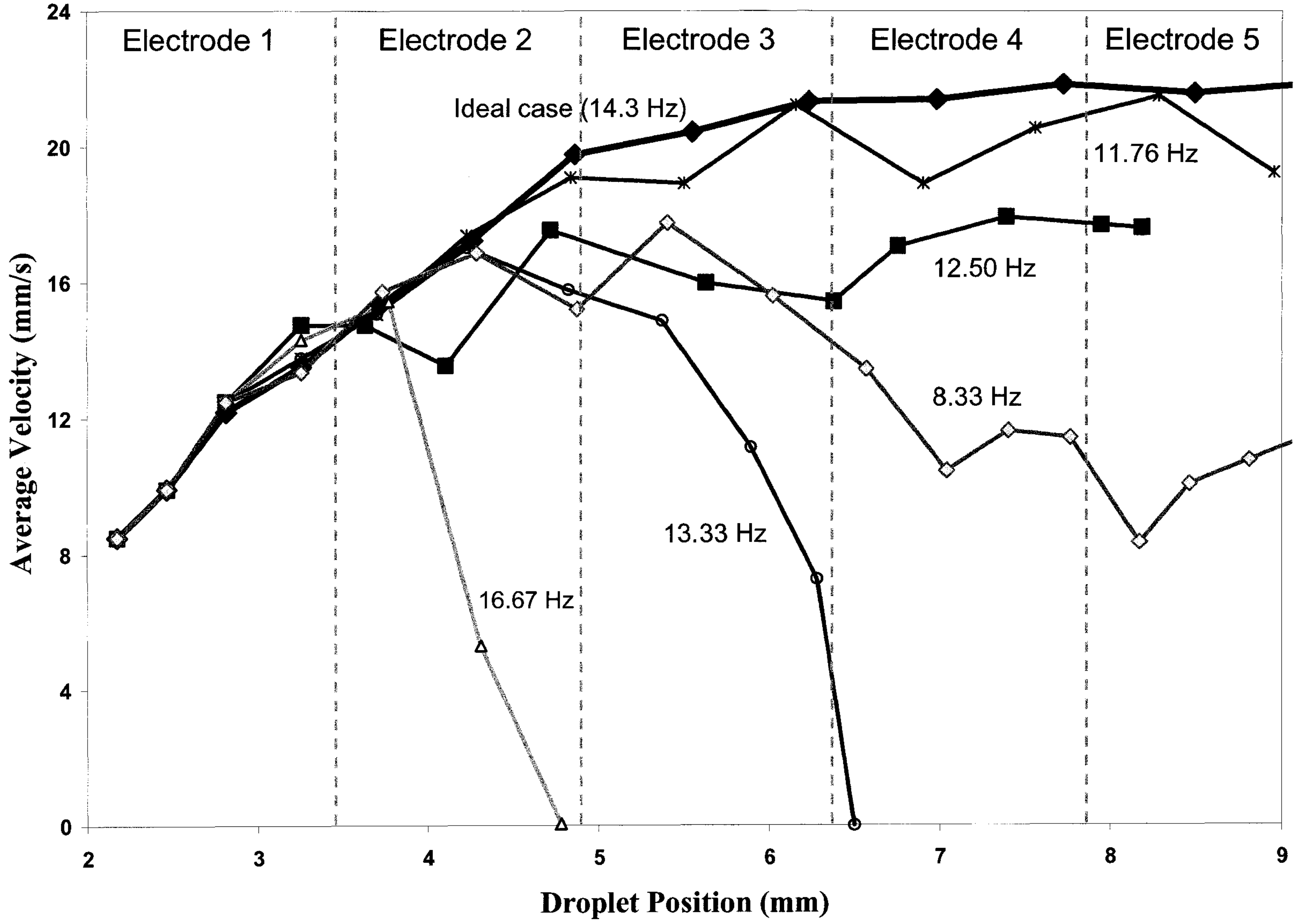

Figure 4-11. The effect of electrode switching frequency on the droplet velocity

In all cases, the droplet accelerates within the first and some times the second electrode. If the switching time is suitable enough, the droplet continues moving. As an example, the switching frequency of 11.8 Hz results in a velocity pattern close to the ideal one. The difference is that the velocity will not become steady and it fluctuates but with the values near to the maximum velocity. In the case of 12.5 Hz, although the droplet continues to move, its velocity drops to the value of about 16-18 mm/s and it fluctuates.

When the timing is not proper, the droplet stops in the middle of the channel. This is due to the fact that the cause of motion is the electric force and if the current electrode is switched off while the droplet still has a remarkable distance to travel to reach the end of the electrode, its inertia would not be sufficient to pull it all the way to reach to the next electrode which has been switched on. As a result, it stops after some times. This happens with the frequencies of 13.3 and 16.7 Hz, one more than the ideal frequency and one less than that.

By decreasing the frequency, which means delaying the time that each electrode is powered, one may manage to decrease the velocity of the droplet. For instance, the switching frequency of 8.3 Hz leads to a fluctuating velocity. In that case, the velocity drops while oscillating but for the current channel length, 90 mm, it does not stop.

The frequency study shows various droplet behaviors while facing different switching frequencies. This concept can be used for design and fabrication of microdevices actuated by electrowetting. In addition, it can be a means of controlling the droplet motion and velocity through the channel.

4.5 Electrode size effect

Figure 4-12 shows the change of droplet velocity with position along the channel. The actuation voltage is 60V. The droplet starts accelerating when it is still on the first electrode. The velocity reaches to a steady state condition after a while. The graph shows the velocity curve for three different electrode sizes. It shows that by increasing the electrode size the ultimate velocity increases as well. However, it should be noted that the velocity will decrease due to the backward force, if the electrode size is larger than the droplet size. Therefore, there is always a limit for increasing the electrode size.

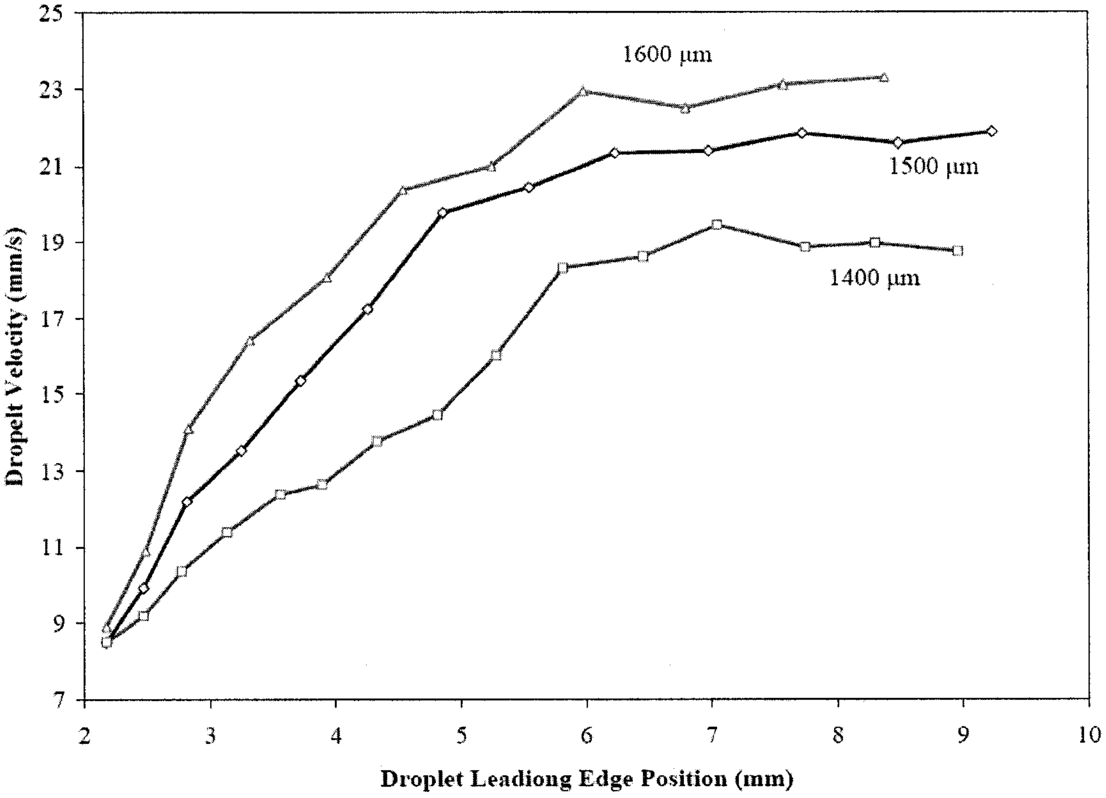

Figure 4-12. Droplet leading edge velocity with respect to the electrode size

5. Conclusions and Future Work

5.1 Conclusions

The droplet behaviour under the electrowetting actuation in microchannels was investigated. Since the problem involves free surface flows, the Volume of Fluid (VOF) method was applied to solve for the location of the interface along with the flow governing equations. A numerical algorithm was added to the flow governing equations to solve for the electric field. The equations are solved simultaneously and the effect of the imposed electric field was captured by calculating the electric forces which then were fed to the Navier-Stokes equation as the actuation forces at every timestep.

Different aspects were studied to predict the behaviour of the droplet under the electrowetting actuation. The droplet deformation at the beginning of the actuation, while approaching the first powered electrode was discussed. In addition, the contact line deformation was shown at each step. Droplet morphology was investigated while traveling on the first electrode (the advent of actuation) as well as on a series of electrodes inside a channel.

The droplet velocity along the channel was calculated for different actuation voltages. These results were compared with the existing experimental data in the literature. The numerical results showed acceptable consistency with the experimental data. The existing deviation is believed to be due to the influence of the contact angle hysteresis. A maximum velocity of 22 mm/s was calculated for the actuation voltage of 60V. In addition, the droplet leading edge, trailing edge, and the instantaneous velocities are discussed.

For the design purposes, different electrode switching frequencies were examined. Their effects on the droplet motion were investigated in detail. Different velocity pattern may be achieved by changing the switching frequency. The droplet velocity may start to fluctuate, decrease, or even drop to zero for certain frequencies; while, in the ideal case, it accelerates and reaches to a steady state value.

Finally, the effect of electrode length on the droplet velocity is studied. It was shown that by changing the electrode shape from squares to rectangles with smaller length but the same width as before, one can improve the actuation. However, there exists a limit for the electrode length; it should not be larger than the droplet diameter. This is to prevent the possible backward actuation effects that can slow down the droplet while traveling along the channel.

5.2 Future work

There are many opportunities to continue working in this field. This work serves as a start for the numerical simulations for design the electrowetting-actuated devices. Some other phenomena such as contact angle hysteresis and contact angle saturation should be studied and added to the current model so that it includes several effects and consequently to improve the results.

The contact angle hysteresis effect has been modeled by shifting the results in the current work. A more sophisticated model which considers the various physical aspects such as the surface roughness and heterogeneity would certainly result in more realistic simulations.

In reality, there is a limit to increase the voltages. It has been observed that the contact angle decreases by increasing the voltage. However, after a certain angle, further increase in the voltage does not yield in the contact angle change. This is so called contact angle saturation [24]. Few studies have been performed in the literature to explain the phenomenon and more is needed to be able to model it numerically. Adding this effect also will help to attain more realistic results in simulations.

In this work, the contact angle is considered to be static. It should be noted that in fact this angle is dependent on the contact line velocity. This is called dynamic contact angle. More studies should be performed to link the contact line velocity to the values of the contact angle in the contact line.

And Finally, Lab-on-a-chip devices are used basically in biochemistry and biotechnology where most of the samples such as proteins, blood, buffers, and other biochemical reagents behave as non-Newtonian fluids. These fluids cannot be studied with the actual governing equations because of their particular characteristics. Both the flow and electrical equations are needed to be modified for every sample to be examined.

References

---

1 Dongqing Li, “Electrokinetics in Microfluidics” Elsevier Academic Press, 2004

2 S. Shoji, M. Esahi, Microflow devices and systems, J. Micromech. Microeng., 4:157-171, 1994

3 P. Gravesen, J. Branebjerg, and O. S. Jensen, Microfluidics – a review. J. Micromech. Microeng., 3:168-182, 1993

4 D. T. Burk, M. A. Burns, and C. Masterangelo, Microfabrication technologies for integrated nucleic acid analysis, Genome Research, 7:189-197, 1997

5 M. A. Burns et al. An integrated, nanoliter DNA analysis device, Science. 282:484-487, 1998

6 M. K. Chaudhury and G. M. Whitesides, How to make water run uphill, Science, 256:1539-1541, Jun. 1992

7 A. W. Adamson and A. P. Gast, Physical Chemistry of Surfaces, John Wiley and Sons, Inc., 6th edition, 1997

8 E. B. Dussan, On the spreading of liquids on solid surfaces: static and dynamic contact lines, Ann. Rev. Fluid Mech. 11:371-400, 1979

9 G. O. Berim, E. Ruckenstein, microscopic interpretation of the dependence of the contact angle on roughness, Langmuir 21: 7743-7751, 2005

10 N. A. Patankar, On the modeling of hydrophobic contact angles on rough surfaces, Langmuir 19: 1249-1253, 2003

11 B. S. Gallardo et al. Electrochemical principles for active control of liquids on submillimeter scales, Science, 283:57-60, Jan. 1999

12 K. Ichimura, S. Oh, and M. Nakagawa, Light-driven motion of liquids on a photoresponsive surface, Science, 288:1624-1626, 2000

13 T. S. Sammarco and M. A. Burns, Thermocapillary pumping of discrete drops in microfabricated analysis devices, AIChE J., 350-366, 1999

14 T. S. Sammarco and M. A. Burns, Heat-transfer analysis of microfabricated thermocapillary pumping and reaction devices, J. Micromech, Microeng., 10:42-55, 2000

15 G. Beni, S. Hackwood, and J. L. Jackel, Continuous electrowetting effect, Appl. Phys. Lett., 40(10):912-914, 1982

16 J. Lee, C. J. Kim, Liquid micromotor driven by continuous electrowetting, In proc. of IEEE MEMS 98, Heidelberg, Germany, 538-543, Jan. 1998

17 J. L. Jackel, S. Hackwood, and G. Beni, Electrowetting optical switch, Appl. Phys. Lett., 40(1):4-6, 1982

18 M. Washizu, Electrostatic actuation of liquid droplets for microreactor applications, IEEE Transaction on Industry Applications, 34(4):732-737, 1998

19 M. G. Pollack, “Electrowetting-based microactuation of droplets for digital microfluidics”, PhD thesis, Duke University, Durham, NC, USA, 2001

20 M. G. Pollack, A. D. Shenderov, R. B. Fair, “Electrowetting-based actuation of droplets for integrated microfluidics”, Lab Chip, 2: 96-101, 2002

21 S. K. Cho, H. Moon, C. J. Kim, “Creating, transporting, cutting, and merging liquid droplets by electrowetting-based actuation for digital microfluidic circuits”, Journal of Microelectromechanical Systems, Vol. 1, No. 1, Feb. 2003

22 Vers Un Démonstrateur intégré pour l’Analyse Chimique ou Biologique sur Site, Dossier, La revu trimestrielle du réseau Ecrin, N° 61 Sep. 2005

---

23 J. Zeng, T. Korsmeyer, Principles of droplet electrohydrodynamics for lab-on-a-chip, Lab on a chip 4: 265-277, 2004

24 B. Shapiro, H. Moon, R. Garrell, C. J. Kim, Equilibrium behaviour of sessile drops under surface tension applied external fields and material variations, J. Appl. Phys. 93, No. 9, 2003

25 V. Bahadur, S. V. Garimella, "En energy-based model for electrowetting-induced droplet actuation", J. Micromech. Microeng. 16: 1494-1503, 2006

26 E. Baird, P. Young, K. Mohseni, Electrostatic force calculation for an EWOD-actuated droplet, Microfluid Nanofluid, Springer-Verlag 2007 (Accepted 2 Dec. 2006)

27 J. Berthier, P. Dubois, P. Clementz, P. Claustre, C. Peponnet, Y. Fouillet, "Actuation potentials and capillary forces in electrowetting based microsystems", Journal of Sensors and Actuators A: Physical, V.134, Issue 2, 471-479, 2007

28 A. Dolatabadi, K. Mohseni, and A. Arzpeyma, "Behaviour of a moving droplet under electrowetting actuation: Numerical simulation", Canadian Journal of Chemical Engineering, Volume 84, number 1:17-21, 2006

29 A. Dolatabadi, K. Mohseni, and P. Wood-Adams, "Modeling electrowetting-based droplet actuation in microchannel", 20th Canadian Congress on Applied Mechanics, CANCAM 2005, pp 538-539, May 30-June 2, 2005, Montreal, Quebec, Canada

30 K. Mohseni and A. Dolatabadi, "An electrowetting micro-valve: Numerical simulation", in press, Annals of the New York Academy of Sciences (2006)

31 Y. Kao and Y. Sato, "Measurement of electric double layer between electrolyte-glass interface by evanescent wave light illumination", 12th International symposium on application of laser technologies to fluid mechanics, Lisbon, Portugal 2004.

---

32 L. D. Landau and E. M. Lifshitz, Fluid Mechanics, p. 241, Pergamon Prerss, Oxford 2nd edition 1987

33 J. U. Brackbill, D. B. Kothe, and C. Zeamch, A continuum method for modeling surface tension, J. Comptut. Phys. 100:335, 1992

34 M. Bussmann, A Three-Dimensional Model of an Impacting Droplet, PhD Thesis, University of Toronto, 2000

35 M. Bussmann, J. Mostaghimi, S. Chandra. On a three-dimensional volume tracking model of droplet impact. Phys Fluids., Volume 11, Issue 6: 1406-1417, 1999

36 D. B. Kothe, R. C. Mjolsness, and M. D. Torrey, RIPPLE: A computer program for incompressible flows with free surfaces, Technical Report LA-12007-MS. LANL. 1991

37 D. B. Kothe, R. C. Mjolsness, RIPPLE: A new model for incompressible flows with surface tension, AIAA J., 30:2694, 1992

38 F. H. Harlow and J. E. Welch, Numerical calculation of time-dependent viscous incompressible flow of fluid with free surface, Phys. Fuids, 8(12):2182-2189, 1965

39 J. E. Welch, F. H. Harlow, J. P. Shannon, and B. J. Daly, The MAC method, Technical Report LA-3425, LANL, 1966

40 J. H. Ferziger and M. Perić, Computational Methods for Fluid Dynamics, Springer, Berlin, 1997

41 B. van Leer, Towards the ultimate conservative finite difference scheme IV, J. Comput. Phys., 32:101, 1979

42 W. J. Rider and D. B. Kothe, Reconstructing volume tracking, J. Comput. Phys. , 141:112-152, 1998

Appendix

In this section the two other methods to explain the electrowetting formulation are explained. The first method has been explained in Chapter 2.

Energy minimization method

The shape of a droplet when placed on a solid surface is a function of both the liquid characteristics (solvent, and ionic and surfactant solutes) and the composition and morphology of the solid. Applying an electric potential across the liquid droplet leads to a redistribution of ions and dipoles in the liquid and in the solid or both, depending on the relative material properties.

Shapiro et al.[i] studied the different physical effects such as gravity and electric fields, electrical resistance, and ionic double layer (EDL) on a droplet. Below is a brief explanation of the effect of various fields on the droplet.

---

[i] B. Shapiro, H. Moon, R. Garrell, C. J. Kim, Equilibrium behaviour of sessile drops under surface tension applied external fields and material variations, J. Appl. Phys. 93, No. 9, 2003

In this section we deal with energies instead of forces, as these forces are derivative of a potential energy (conservative forces). Also, the mechanism of raising the force in the tri-phase contact line and its relation with the ion diffusion at this area is not known. So here we deal with potential energy associated with an ion distribution field.

The geometry investigated here is a droplet sitting on a hydrophobic plate. It is assumed to be a perfect sphere truncated at the solid plate. We also assume that the gravitational and electric fields are small enough so that the droplet does not squash. As the third assumption, we consider there is no deformation at the tri-phase contact line because we are only interested in the bulk shape of the droplet and not the local changes. By these assumptions we can define the shape of the droplet just by two parameters: the radius R and the contact angle θ.

At equilibrium the droplet has a shape with minimized energy E which means that the derivative of the energy with respect to R and θ (shape factors) is zero:

$$dE = \left[\frac{\partial E}{\partial R}(R,\theta;p)\right]dR + \left[\frac{\partial E}{\partial \theta}(R,\theta;p)\right]d\theta = 0 \qquad \text{(a - 1)}$$

here p is a system parameter such as an applied voltage. This relation states that the infinitesimal change in energy must be zero and any change in one R or θ leads to a change of the other one. This means if θ increases, R must decrease to keep the droplet volume constant. The droplet volume is calculated as follow:

$$V(R,\theta) = \pi R^3\left(\frac{2}{3} - \frac{3\cos\theta}{4} + \frac{\cos 3\theta}{12}\right) \qquad \text{(a - 2)}$$

As the volume is constant, its derivative is zero and the relation between R and θ can be found easily:

$$dR = Rq(\theta)d\theta = R\left(-\frac{2\cos^2(\theta/2)\cot(\theta/2)}{2+\cos\theta}\right)d\theta \tag{a - 3}$$

Now we can calculate the change in energy with contact angle by applying equations (1-1) and (a - 3):

$$\left(-\frac{2+\cos\theta}{2\pi R^2\sin\theta}\right)\frac{dE}{d\theta} = \left(-\frac{2+\cos\theta}{2\pi R^2\sin\theta}\right)\left(\left[\frac{\partial E}{\partial R}(R,\theta;p)\right]Rq(\theta) + \left[\frac{\partial E}{\partial R}(R,\theta;p)\right]\right) = 0 \tag{a - 4}$$

In Equation (a - 4), to reach to the traditional Young equation, the equation is multiplied by a strictly non-zero negative term of $-(2+\cos\theta)/2\pi R^2\sin\theta$. If E includes only interfacial energies of liquid-solid, liquid-gas, and solid-gas with a constant surface tension, Equation (a - 4) becomes exactly Young's equation.

By assuming a linear electric field where $E = V/d$ in dielectric (E is the electric field, V the applied voltage, and d is dielectric thickness) and neglecting the edge effects, the stored energy in dielectric may be calculated as follow:

$$E_{de}(R,\theta) = \frac{1}{2}\varepsilon\left(\frac{V}{d}\right)^2 dA_{ls} = \frac{\varepsilon V^2}{2d}\pi R^2\sin^2\theta \tag{a - 5}$$

Combining Equations (a - 4) and (a - 5) we find the Young-Lippmann equation:

$$\cos\theta - \left(\frac{\gamma_{gs}-\gamma_{ls}}{\gamma_{\mathrm{lg}}} + \frac{\varepsilon V^2}{2\gamma_{\mathrm{lg}}d}\right) = 0 \tag{a - 6}$$

The electromechanical approach

In this approach, the electrohydrodynamic, EHD, forces are calculated. The electric properties of a fluid inside an electric field may be described by the following constitutive law[ii]:

$$E = E(\alpha_1, \alpha_2, \ldots, \alpha_m, D) \qquad \text{(a - 7)}$$

where E is the electric field, D is the electric displacement , and α_i is the material property of the fluid. The EHD force density exerted on the fluid is:

$$f^e = \rho_e E - \sum_{i=1}^{m} \alpha_i \nabla\left(\frac{\partial W}{\partial \alpha_i}\right) \qquad \text{(a - 8)}$$

where ρ_e is the volumetric charge density and W is the volumetric density of the electric energy defined as:

$$W = \int_0^D E(\alpha_1, \alpha_2, \ldots, \alpha_m, D')\,dD' \qquad \text{(a - 9)}$$

Equation (a - 8) shows that there are two different electric forces acting on the fluid: the first term is the Coulombic force, which is due to the existence of free charges in the bulk or at the interface; the second term is the dielectrophoresis, DEP, force which is due to the effect of electric properties of the material.

No free charge exists in the two-fluid interface as its normal is perpendicular to the electric field E; so the free charges are only at the droplet-insulator interface. The surface charge density may be written as:

[ii] J. R. Melcher, Continuum electromechanics, The MIT Press, 1981, Section 3.7

$$\sigma_{sl} = \varepsilon_0 \varepsilon \frac{\psi_{sl}}{d} \qquad \text{(a - 10)}$$

where ψ_{sl} is the electric potential at the liquid-solid interface and d is the insulator thickness.

For a specified control volume, the electric force can be calculated by differentiating the energy in the direction of displacement:

$$F = \nabla_{\xi} \int W dV \qquad \text{(a - 11)}$$

The integral is over control volume and the gradient is with respect to the material displacement ξ.

The EHD force at the two-fluid interface may be found as:

$$F_1 = -\frac{\varepsilon_a \psi^2}{8d^2} \frac{\left(\frac{2d}{h}\right)^2}{\left(1 + \frac{2d}{h}\frac{\varepsilon_a}{\varepsilon_i}\right)^2} \qquad \text{(a - 12)}$$

where h is the channel gap size and the subscripts a and i refer to the ambient medium and the insulator. The EHD force acting on the tri-phase contact line is as:

$$F_2 = \frac{\varepsilon_i \psi^2}{8d^2} \left(1 - \frac{1}{\left(1 + \frac{h}{2d}\frac{\varepsilon_i}{\varepsilon_a}\right)^2} \right) \qquad \text{(a - 13)}$$

The latter force is in the tri-phase contact line plane and perpendicular to this line while pointing away from the droplet. Usually, in real cases, the ratio of the dielectric thickness to the channel gap d/h is very small. In our case d = 900 nm and h is about 300 μm. Therefore, we can consider the ratio to be zero. By this assumption F_1 becomes zero which means that with such ranges of gap size and insulator thickness, the value of the electric force on the two-fluid interface is negligible.

The other term of the electric force can be simplified as:

$$F_2 = \frac{\varepsilon_i \psi^2}{8d^2} \qquad \text{(a - 14)}$$

This force term along with Young equation gives the same result of contact angle changes as of Equation (2-3).

Here the force terms regarding the effect of dipole moments are not mentioned. These forces are called the dielectrophoresis force DEP and exist when the liquid is dielectric itself which is not the case in electrowetting.